Erasmus+: Erasmus Mundus Joint Master Degree
programme AstroMundus in Astrophysics

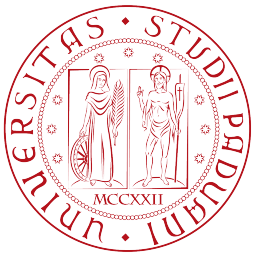

Università degli Studi di Padova
Dipartimento di Fisica e Astronomia "Galileo Galilei"
Corso di Laurea Magistrale in Astronomia

Bispectrum of the Sunyaev-Zel'dovich y-Compton Field in Modified Gravity Models

Relatore:
Dott. Michele Liguori
Correlatore:
Andrea Ravenni

Studente:
Slađana Radinović
Matricola:
1158302

Anno Accademico 2017/2018

Contents

Introduction

The accelerated expansion of the universe was first discovered by Edwin Hubble, while observing the redshifts of distant galaxies. Since then, we have tried to explain this expansion. One way to do it is using the ΛCDM cosmological model, developed in the framework of general relativity. This model explains expansion by introducing a new form of energy, called "dark energy". Though ΛCDM has achieved great success in explaining observations, the exact nature of dark energy still remains a mystery. While it is widely believed it is in the form of a cosmological constant, there are also models proposing that it is a time-evolving scalar field, or quintessence.

There is, however, another way to describe the accelerated expansion. Modified gravity models, for example, explain it by making a modification to general relativity on large scales. In this thesis, we will explore one class of these models, called $f(R)$ models. Modifying gravity, of course, will have an impact on the gravitational collapse of massive objects. Being the biggest gravitationally bounded objects in the universe, galaxy clusters are the most suitable candidates to detect small deviations from general relativity. We will in particular use one of the late-time anisotropies observed in the cosmic microwave background, the thermal Sunyaev-Zel'dovich effect. As it directly traces galaxy clusters, it represents a good probe for the large scale structure.

We will specifically use the two- and three-point correlation functions of the thermal Sunyaev-Zel'dovich effect — its power spectrum and bispectrum. Since the evolution of large scale structure has made the matter distribution non-Gaussian, we expect a lot of information to be contained in the bispectrum, which is why it is the main focus of this thesis.

Our goal is, therefore, to calculate and analyze the power spectrum and bispectrum of thermal Sunyaev-Zel'dovich effect, and to do a Fisher forecast for an ideal, cosmic variance limited experiment. The forecast will enable us to see how well we can constrain $f(R)$ modified gravity models. In the future we hope to compare our results to *Planck* data, and provide constraints on the $f(R)$ parameter, f_{R0}.

The thesis is structured as follows.

In **Chapter 1** we give a brief overview of cosmology and introduce general relativity as a framework for describing the universe. We also introduce the expansion of the universe, as well as the current cosmological model used to explain it, ΛCDM.

Chapter 2 describes the formation and evolution of large scale structure using the halo model. Here we explain how dark matter halos are formed in the

context of spherical collapse, and we study the halo mass function.

In **Chapter 3** we introduce the CMB and take a quick look at the temperature distribution and anisotropies present in it. We study some of the physical mechanisms leading to these anisotropies, especially the main focus of this thesis — the thermal Sunyaev-Zel'dovich effect.

Chapter 4 provides an alternative explanation for the accelerated expansion of the universe in the form of modified gravity. Here we focus specifically on the Hu-Sawicki $f(R)$ model and how it modifies the halo model theory described in Chapter 2.

Chapter 5 briefly introduces the notion of a Fisher forecast. It also looks at spherical decomposition of observables on a sphere, specifically the power spectrum and bispectrum, and their covariances.

In the final chapters we present our results.

Chapter 6 briefly describes the calculation of the power spectrum and the bispectrum of the Sunyaev-Zel'dovich effect, using the halo model. Here we give results for both general relativity and modified gravity.

In **Chapter 7** we present the results of our Fisher forecast, using the Sunyaev-Zel'dovich bispectrum. We give bispectrum derived constraints on some cosmological and intra-cluster medium parameters, as well as the modified gravity parameter f_{R0}. We note the potential to break the degeneracies between some parameters by a combined analysis of the power spectrum and bispectrum.

Chapter 1

Introduction to Cosmology

> "There is a theory which states that if ever anyone discovers exactly what the Universe is for and why it is here, it will instantly disappear and be replaced by something even more bizarre and inexplicable."
>
> – Douglas Adams, *The Restaurant at the End of the Universe*

From the moment they became aware of the world surrounding them, humans have had a desire to try and explain it. These attempts mark the first steps in cosmology. Even today, millennia later, we are still working hard on this task. Though our questions become more and more complicated and specific, the core goal remains the same: understanding the universe.

The basis of our theories today is the Copernican principle which states that the Earth is not in a very special place in the Universe. Expanding this view into the **cosmological principle**, we say that we can expect the physics that is at work in our cosmic backyard to be the same in other places in the universe as well. If we were then to observe that the universe seems rather homogeneous and isotropic from our point of view, we could safely assume that it is that way everywhere.

It might seem strange to assume that the universe is indeed like this, after all we see inhomogeneities every day. A cat, for example, is very different from a rock, and they are both even more different from the center of the Sun, or the cold vacuum of space. One look at the Cosmic Microwave Background, however, tells us that on large enough scales the matter distribution in the universe really is homogeneous and isotropic.

1.1 Distances in an Expanding Universe

An important piece in our understanding of the universe came with the discovery that it is expanding. Unlike in static, flat space that we are used to, even the simple task of measuring distances now required some finesse.

Consider the points on a square grid in Figure 1.1, with sides of unit length. We define two measures of distance: a proper one, and a comoving one. The comoving distance χ, as the name suggests, moves with the grid; if the grid

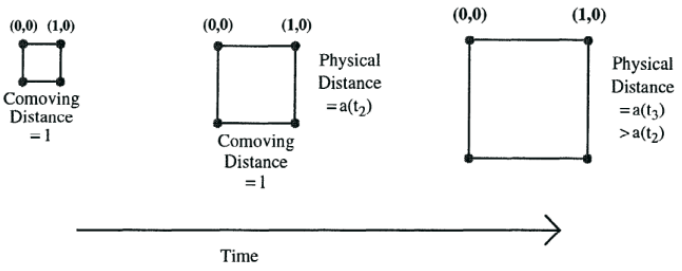

Figure 1.1: Illustration of the expansion of the universe (Dodelson, 2003).

stretches in any way, the comoving distance between two points remains the same, one unit length. On the other hand, the proper, physical distance d changes depending on how much the grid stretches or shrinks. This is illustrated by the time dependent **scale factor** $a(t)$, a dimensionless quantity that is normalized in such a way that it is unity at present time.

We can now relate the proper distance to the comoving one:

$$d(t) = a(t)\chi\,. \tag{1.1}$$

So what do we expect to see when we look out into the expanding universe around us? Since space is expanding everywhere at once, while standing here on Earth it seems that everyone in the universe is moving away from us! Since light emitted from objects that are moving away is redshifted, we can define a cosmological **redshift** z as:

$$1 + z = \frac{\lambda_{\rm obs}}{\lambda_{\rm em}} = \frac{1}{a(t)}\,, \tag{1.2}$$

where $\lambda_{\rm em}$ is the initial wavelength emitted by some object, and $\lambda_{\rm obs}$ is the redshifted wavelength we observe.

Observing redshifts of distant galaxies is exactly how Edwin Hubble first noticed that these galaxies appear to be moving away (Hubble, 1929). Moreover, they seemed to be moving away faster the more distant they were, a trend that can be seen in the Hubble diagram, in Figure 1.2. This was the first direct evidence that the universe is indeed expanding.

If we now assume the movement of the galaxies is only due to expansion, or the Hubble flow, we can say that their velocity is:

$$v = \dot{d} = \dot{a}\chi = \frac{\dot{a}}{a}d = Hd\,, \tag{1.3}$$

where

$$H \equiv \frac{\dot{a}}{a} \tag{1.4}$$

is the **Hubble constant**, and represents the slope of the velocity-distance relation in the Hubble diagram.[1]

[1]Note that we have used Newton's notation, where the overdot signifies a derivative with respect to time.

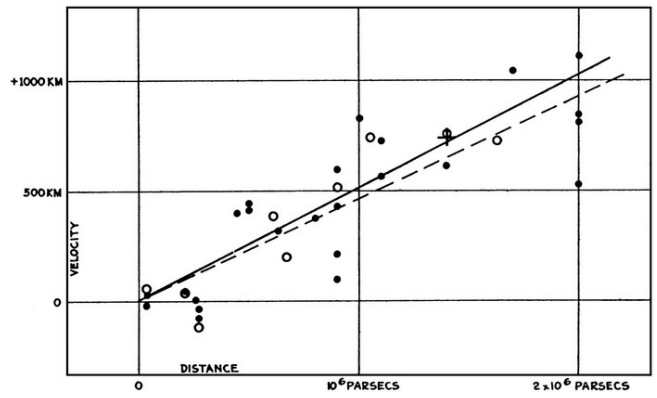

Figure 1.2: The Hubble diagram (Hubble, 1929). The units are km $\sec^{-1}$ for velocity and Mpc for distance.

So how do we go about measuring distances? One way is to use an object of known size, l, and compare it to its angular size as seen from Earth, θ. Knowing that, in a flat universe, angle θ is given by the ratio of the size of the object and its physical distance, and using eq. (1.1), we get the **angular diameter distance**:

$$d_{\mathrm{A}} = \frac{l}{\theta} = a\chi = \frac{\chi}{1+z}\,. \tag{1.5}$$

Another way to measure distance is using an object of known luminosity L and observed flux F:

$$F = \frac{L}{4\pi d_{\mathrm{L}}}\,, \tag{1.6}$$

where d_{L} is the **luminosity distance**. In an expanding universe the observed flux coming from the object is reduced thanks to two effects:

1. due to expansion, two photons passing through a unit area, δt time apart, will, at a later time, pass a unit area $(1+z)\delta t$ time apart, thus reducing the number of photons going through a unit area in unit time;
2. due to redshift, the energy of photons going through a unit area in unit time is also reduced.

This results in the luminosity distance being:

$$d_{\mathrm{L}} = \chi\,(1+z)\,. \tag{1.7}$$

1.2 General Relativity

A fundamental tool in our quest to describe the universe is Einstein's theory of General Relativity. Developed in the early 1900s, Einstein's theory presented an elegant, geometrical explanation for gravity, in which matter was directly influenced by the spacetime upon which it was set. It states that gravity is only an effect of curvature in spacetime, or as John Wheeler put it: "*Spacetime tells matter how to move; matter tells spacetime how to curve*" (Wheeler and Ford, 1998).

General relativity (GR) describes spacetime as a manifold. Simply put, an n-dimensional manifold is used to describe a space that locally looks like an n-dimensional Euclidean space. For example, on a small enough scale, the surface of the Earth looks flat (Euclidean), but we already know that the Earth is a sphere. The surface of a sphere is, therefore, an example of a 2-dimensional manifold.[2]

Another thing we impose on our manifold is a **metric**. The metric tensor describes the geometrical properties of a manifold and allows us to easily measure distances. This might seem trivial in a flat Euclidean space but, as we saw in the previous section, curvature in spacetime can complicate things.

To see how a metric looks like, we can take a simple metric for a flat spacetime, the Minkowski metric. It has the following form:

$$g_{\mu\nu} = \begin{pmatrix} -1 & & & \\ & 1 & & \\ & & 1 & \\ & & & 1 \end{pmatrix}, \tag{1.8}$$

so a line element is then:

$$ds^2 = g_{\mu\nu} dx^\mu dx^\nu = -dt^2 + dx^2 + dy^2 + dz^2 \,. \tag{1.9}$$

Before we continue, let us pause for a second to consider some conventions that were used in the above equation. The fact that the time component here has a negative sign shows that we have chosen the spacelike sign convention for the metric, $(-,+,+,+)$, common in cosmology. Additionally, we have omitted a sum in the first part of the equation. This is following Einstein's summation convention which states that we assume a sum over any indices that are repeated (in our case μ and ν). Finally, we are working in natural units, meaning we have set $\hbar = c = k_B = 1$.

For a general metric, we can describe curvature starting with the Riemann tensor, which is a function of the second derivative of the metric:

$$R_{\rho\sigma\mu\nu} = \frac{1}{2} \left(\partial_\mu \partial_\sigma g_{\rho\nu} - \partial_\mu \partial_\rho g_{\nu\sigma} - \partial_\nu \partial_\sigma g_{\rho\mu} + \partial_\nu \partial_\rho g_{\mu\sigma} \right) \tag{1.10}$$

From here we can get the trace of the Riemann tensor — the Ricci tensor:

$$R_{\mu\nu} = R^\lambda{}_{\mu\lambda\nu} \,, \tag{1.11}$$

and *its* trace — the Ricci scalar:

$$R = R^\mu{}_\mu \,. \tag{1.12}$$

Now that we are a little more familiar with some mathematical concepts used in GR, we can actually apply them to gravity. This is where Einstein's equations come in. One way to derive them would be to start from the Einstein-Hilbert action:

$$S = \int d^4x \sqrt{-g} \left(\frac{R}{16\pi G} + \mathcal{L}_\mathrm{m} \right), \tag{1.13}$$

[2]This explanation of a manifold is greatly simplified, but serves well for the purpose of this thesis.

where g is the trace of the metric tensor, R is the Ricci scalar, G is the universal gravitational constant, and $\mathcal{L}_{\mathrm{m}}$ is the Lagrangian of the matter content of the universe. Varying the action with respect to $g_{\mu\nu}$, through the principle of least action(Hilbert, 1915), we can get **Einstein's field equations**:

$$R_{\mu\nu} - \frac{1}{2} R\, g_{\mu\nu} = 8\pi\, G\, T_{\mu\nu}\,. \tag{1.14}$$

The right hand side here describes the matter content of the universe, with the energy-momentum tensor $T_{\mu\nu}$, while the left hand side describes the curvature of spacetime, using the Ricci scalar and tensor.

Einstein himself tried to find a solution to these equations, that would give a matter dominated static universe. Since matter self gravitates, however, the solution resulted in a collapsing universe. To correct for this, Einstein added an additional term to the left hand side – $\Lambda\, g_{\mu\nu}$. The goal of this term was to counteract the gravitational collapse, and the scalar quantity Λ was dubbed the cosmological constant. Eventually, as the universe was proven not to be static after all, Einstein once again took the cosmological constant out of the equation. This, however, only lasted until the late 1990s, as evidence of accelerated expansion (Riess et al., 1998; Perlmutter et al., 1999) brought it back into the picture.

1.3 FLRW Metric and the ΛCDM Model

If we want to use General Relativity to describe our universe, we must first choose an appropriate metric. We've already stated that the universe is expanding and that the matter distribution is homogeneous and isotropic.

A metric that describes this kind of a universe was first introduced by Alexander Friedmann (Friedmann, 1922), and is now known by the name Friedmann-Lemaître-Robertson-Walker metric, or FLRW for short. In spherical coordinates, the line element has the following form:

$$ds^2 = -dt^2 + a^2(t)\left(\frac{dr^2}{1-\kappa r^2} + r^2 d\Omega^2\right), \tag{1.15}$$

where $a(t)$ is the already mentioned scale factor, and κ describes the curvature of space. For flat space $\kappa = 0$, and we will see later that this is indeed the case for our universe. For now, however, we will keep κ and consider the general form of the metric.

Using eq. (1.14), we can build the field equations for the FLRW metric. The first ingredients are the Ricci scalar and Ricci tensor. From the definitions in equations (1.10)–(1.12), we find that the only non-zero components of the Ricci tensor are:

$$R_{00} = -3\frac{\ddot{a}}{a}\,, \tag{1.16}$$

$$R_{ij} = \left(\frac{\ddot{a}}{a} + 2\frac{\dot{a}^2}{a^2} + 2\frac{\kappa}{a^2}\right) g_{ij}\,, \tag{1.17}$$

and the Ricci scalar is then:

$$R = 6\left(\frac{\ddot{a}}{a} + \frac{\dot{a}^2}{a^2} + \frac{\kappa}{a^2}\right). \tag{1.18}$$

Index 0 here signifies the time component, and the Latin letters signify spatial components. Similarly, $g_{\mu\nu}$ represents the full spacetime metric, while g_{ij} is only the spatial part.

Now we need to put some energy into our universe. Assuming we have something close to an ideal fluid, with energy density ρ, pressure p and four-velocity u_μ, we write the energy-momentum tensor as:

$$T_{\mu\nu} = (\rho + p)u_\mu u_\nu + p g_{\mu\nu}\,, \tag{1.19}$$

Usually we assume a simple relation between p and ρ, and write the equation of state as:

$$p = w\rho\,, \tag{1.20}$$

where w is a parameter that depends on the type of fluid we are considering.

Putting these definitions into eq. (1.14), and doing a little bit of math, we get two differential equations:

$$H^2 = \left(\frac{\dot{a}}{a}\right)^2 = \frac{8\pi G}{3}\rho - \frac{\kappa}{a^2}\,, \tag{1.21}$$

$$\frac{\ddot{a}}{a} = -\frac{4\pi G}{3}\rho\,(1 + 3\,w)\,. \tag{1.22}$$

These are the **Friedmann equations** and they describe the evolution of the scale factor, relating it to the energy density in the universe. We see that in case of a flat universe ($\kappa = 0$), the energy density would be:

$$\rho_c = \frac{3H^2}{8\pi G}\,. \tag{1.23}$$

We call this the critical density (hence the subscript) and use it to define a dimensionless density parameter, $\Omega = \frac{\rho}{\rho_c}$. This way we can relate the energy content of the universe to curvature.

$$\Omega < 1 \rightarrow \qquad \kappa < 0 \rightarrow \qquad \text{open universe} \tag{1.24}$$

$$\Omega = 1 \rightarrow \qquad \kappa = 0 \rightarrow \qquad \text{flat universe} \tag{1.25}$$

$$\Omega > 1 \rightarrow \qquad \kappa > 0 \rightarrow \qquad \text{closed universe} \tag{1.26}$$

Current observations of the CMB are consistent with a flat universe(Aghanim et al., 2018), meaning that the energy density is close to the critical one and we can set $\kappa = 0$.

So far we have not specified what exactly *is* the energy content of the universe. Ω simply denotes the total density and is in fact a mixture of several components. Currently, the best cosmological model is the ΛCDM model, and it states that the universe is made up of:

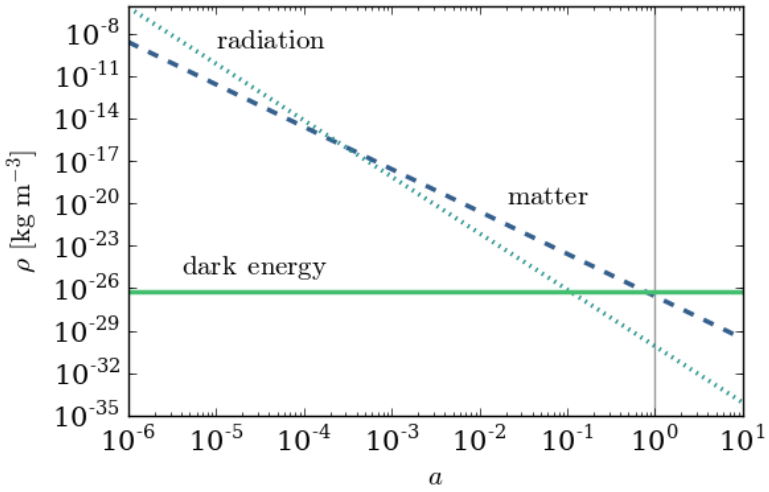

Figure 1.3: Evolution of radiation, matter, and dark energy density parameters with scale factor. The vertical line represents the value of the scale factor today.

1. a matter component (baryonic and cold dark matter), with density parameter Ω_m;
2. a relativistic component (radiation and neutrinos), with density parameter Ω_r and
3. dark energy, with density parameter Ω_Λ.

Now we can write the total density parameter Ω as:

$$\Omega = \Omega_\mathrm{m} + \Omega_\mathrm{r} + \Omega_\Lambda \tag{1.27}$$

All of these components have different equations of state, and thus behave differently. To illustrate this, let us first use the two Friedmann equations to get the energy conservation law for an expanding universe:

$$\dot{\rho} + 3\,\frac{\dot{a}}{a}\,\rho\,(1+w) = 0\,. \tag{1.28}$$

Integrating, we get:

$$\rho \propto a^{-3(1+w)}\,. \tag{1.29}$$

One thing we can immediately see is that for an equation of state parameter $w = -1$, the density is constant in time. This is precisely the case for the cosmological constant. For a pressureless fluid, such as matter, $w = 0$, and for radiation it is $w = \frac{1}{3}$. This difference in energy density evolution means that different components were dominant at different times in the universe's history (Figure 1.3).

Now that we know how the energy density of each of our components evolves, we can divide and multiply eq. (1.21) by the critical density $\rho_{\mathrm{c},0}$, where subscript "0" denotes that we are speaking about the value of a quantity today. For a flat universe ($\kappa = 0$), we then get:

$$H^2 = H_0^2\,\left[\Omega_{0,\mathrm{m}}\,a^{-3} + \Omega_{0,\mathrm{r}}\,a^{-4} + \Omega_\Lambda\right]\,, \tag{1.30}$$

where $H_0^2 = 8\pi G/3\,\rho_{c,0}$ is the present day Hubble parameter.

Assuming that Λ is the dominant term, we can say $\Omega \approx \Omega_\Lambda$ and just consider $H^2 \approx H_0^2 \Omega_\Lambda$. Bearing in mind the definition of the Hubble parameter, eq. (1.4), we can solve this differential equation to get:

$$a(t) \propto e^{Ht}\,. \tag{1.31}$$

This result shows that dark energy really is the driving force behind the accelerated expansion of the universe that we observe today.

Chapter 2

Structure Formation

In the previous chapter we have mentioned that the universe appears homogeneous and isotropic on large enough scales, more specifically at scales above $\sim$ 200 Mpc. Below these scales, however, structure begins to emerge. Figure 2.1 shows a galaxy map from the Sloan Digital Sky Survey, in which every point represents a galaxy. It is easy to see that galaxies cluster together and form the large scale structure.

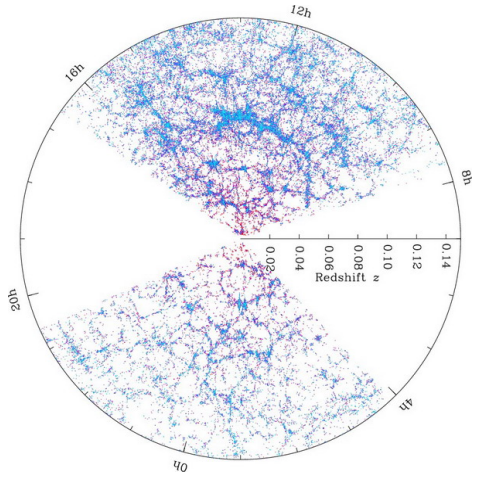

Figure 2.1: Galaxy map from the Sloan Digital Sky Survey (Blanton and SDSS).

Dark matter halos are hosts of galaxy clusters and they represent the largest collapsed structures today. Since halos are observable up to high redshift, they are a great probe of cosmology and we can use them by, for example, relating cosmological parameters to halo abundance. First, however, we need a good theoretical model for halo formation and evolution of abundances.

Since larger structures are the result of small matter density perturbations that grow due to gravitational instability, we will first look at the evolution of these perturbations.

2.1 Linear Perturbation Theory

Density perturbations in the universe can be expressed as fluctuations around the mean density $\bar{\rho}$:

$$\delta_{\mathrm{m}}(\vec{x}) = \frac{\rho(\vec{x}) - \bar{\rho}}{\bar{\rho}}\,, \tag{2.1}$$

where we use the subscript "m" to signify that we are looking at density perturbations of matter (both baryonic and dark). Assuming that the perturbations are small ($\delta_{\mathrm{m}} \ll 1$), as is the case on the largest cosmological scales at early times, we expect their evolution to be linear. This in turn allows us to use linear perturbation theory (Bonnor, 1957; Lifshitz, 1946).

The equations describing the dynamics of a fluid in a gravitational field are:

1. **The continuity equation**, describing the conservation of mass,
2. **Euler's equation**, describing the motion of a fluid with velocity $\vec{u}$, and
3. **Poisson's equation**, describing the gravitational potential ϕ due to a density distribution ρ

Applying these to perturbations (in both density δ_{m} and velocity $\delta\vec{u}$) in an expanding universe, we get:

$$\text{Continuity equation:} \qquad \frac{\partial \delta_{\mathrm{m}}}{\partial t} + \frac{1}{a}\,\nabla \cdot \delta\vec{u} = 0\,; \tag{2.2}$$

$$\text{Euler equation:} \qquad \frac{\partial \delta\vec{u}}{\partial t} + H\,\delta\vec{u} = -\,\frac{1}{a}\,\nabla\phi\,; \tag{2.3}$$

$$\text{Poisson equation:} \qquad \nabla^2\phi = 4\pi G\, a^2\,\bar{\rho}\,\delta_{\mathrm{m}}\,. \tag{2.4}$$

Combining these, we get the differential equation that governs the linear growth of perturbations:

$$\frac{\partial^2 \delta_{\mathrm{m}}}{\partial t^2} + 2H\,\frac{\partial \delta_{\mathrm{m}}}{\partial t} - 4\pi G\,\bar{\rho}\,\delta_{\mathrm{m}} = 0\,. \tag{2.5}$$

As a second-order differential equation, it has two independent solutions, one decaying and one growing in time:

$$\delta_{\mathrm{m}}(\vec{x}, t) = D^{+}(t)\,\delta_i(\vec{x}) + D^{-}(t)\,\delta_i(\vec{x})\,, \tag{2.6}$$

where "+" denotes the growing solution, and "−" is the decaying one. D^{+} is called the linear growth function, while $\delta_i(\vec{x}) = \delta_i(\vec{x}, t_i)$ is the amplitude of the initial perturbations at physical position $\vec{x}$ and initial time t_i.

This solution, as we have stated, holds for the linear regime, while perturbations are small. However, perturbations grow and once δ_{m} becomes comparable to unity linear treatment is not valid anymore. Describing their evolution then requires going to non-linear perturbation theory (Bernardeau et al., 2002) or making some simplifications.

2.2 Spherical Collapse

The simplest way to describe non-linear evolution of perturbations is to assume a spherically symmetric collapse. Consider a flat, matter dominated universe ($\Omega = \Omega_{\rm m} = 1$) — an Einstein-de Sitter universe — with a small initial overdensity $\delta_i \ll 1$, in a region of comoving size R_0. If we have a simple top-hat density profile, the mass contained in this region is:

$$M_0 = \frac{4\pi R_0^3}{3}\,\bar{\rho}\,(1+\delta_i) \approx \frac{4\pi R_0^3}{3}\,\bar{\rho} \tag{2.7}$$

where $\bar{\rho}$ is the comoving background density.

From Birkhoff's theorem (Birkhoff, 1923) we know that we can treat this region as a separate universe so that it's evolution will be independent from the background. The sub-universe then has a density slightly higher then the critical one and evolves like a closed universe, eq. (1.26). The parametrized Friedmann equations for such a universe are given by (Longair, 2008):

$$R_{\rm p} = A\,(\,1-\cos\theta\,)\,, \tag{2.8}$$

$$t = B\,(\,\theta-\cos\theta\,)\,, \tag{2.9}$$

where $R_{\rm p}$ is the scale factor of the sub-universe, and A and B are:

$$A = \frac{\Omega_0}{2(\Omega_0-1)}\,, \tag{2.10}$$

$$B = \frac{\Omega_0}{2H_0(\Omega_0-1)^{3/2}}\,. \tag{2.11}$$

Parameters Ω_0 and H_0 are the density parameter and Hubble constant of the sub-universe.

At some time t, the physical size of the overdense region is $R(z)$ and the parametric solution for it is given by (Cooray and Sheth, 2002):

$$\frac{R(z)}{R_0} = \frac{(1+z)}{(5/3)\,|\delta_0|}\,\frac{(1-\cos\theta)}{2}\,, \tag{2.12}$$

$$(1+z) = \left(\frac{4}{3}\right)^{2/3}\,\frac{(5/3)\,|\delta_0|}{(\theta-\sin\theta)^{2/3}}\,. \tag{2.13}$$

Here we use δ_0 to denote the value of the overdensity today ($t = t_0$) extrapolated from the initial overdensity δ_i using linear theory: $\delta_0 = D(t_0)^+\delta_i$, from eq. (2.6).

The ratio of R_0 and $R(z)$ will then give us the density ratio of our sub-universe with respect to the background. Defining the density contrast as $\Delta = 1+\delta$, we write:

$$\Delta = \frac{\rho}{\bar{\rho}} = \left[\frac{R_0}{R(z)}\right]^3 = \frac{9}{2}\frac{(\theta-\sin\theta)^2}{(1-\cos\theta)^3}\,. \tag{2.14}$$

From equations (2.8) and (2.9), we see that the overdense region expands for values $\theta \in [0,\pi]$, reaching a turnaround point at $\theta = \pi$. From eq. (2.14) we then know that, at turnaround, the average density is 5.55 times larger than that of the background:

$$\left[\frac{R_0}{R_{\rm max}}\right]^3 = \left(\frac{3\pi}{4}\right)^2 \simeq 5.55\,, \tag{2.15}$$

where we denote the maximum extension of the region with $R_{\rm max}$.

After turnaround, the region starts to collapse until $\theta = 2\pi$, at which point the density in the center will be infinite. Of course, in reality, this does not happen; the gas will start to heat, and shocks and pressure gradients will halt the collapse. After virialization, a halo will form with a finite physical radius given by (Coles and Lucchin, 2002):

$$R_{\rm vir} = \frac{R_{\rm max}}{2}\,. \tag{2.16}$$

From turnover to virialization, the overdensity grows by a factor of 2^3 (from eq. (2.16)). At the same time, the background universe expands and the mean density falls off by a factor of 2^2 (using eq. (2.9) and the fact that during matter domination $\rho^{1/3} \propto a \propto t^{2/3}$). The result of this is that a virialized halo will have an overdensity given by:

$$\Delta_{\rm vir} = \frac{\rho_{\rm vir}}{\bar{\rho}} \simeq 5.55 \cdot 8 \cdot 4 = 178\,. \tag{2.17}$$

What is interesting about this result is that it does not depend on the mass nor the formation history of the halo. This means that if we observe a halo with overdensity $\delta_{\rm vir}$, assuming spherical collapse, we can deduce that it is virialized.

Let us try and determine what value for the overdensity we expect from *linear theory*, at the time of virialization. We can write:

$$\delta_{\rm lin}(\theta) = \frac{3}{5}\left(\frac{3}{2}\right)^{2/3}(\theta - \sin\theta)^{2/3}\,, \tag{2.18}$$

so at virialization, for $\theta = 2\pi$, we have:

$$\delta_{\rm c} \simeq 1.69\,. \tag{2.19}$$

This is the critical overdensity needed for spherical collapse. If the linear estimate $\delta_{\rm lin}$ of some overdense region exceeds the critical one, it will collapse into a halo with overdensity $\delta_{\rm vir}$.

It is worth noting that while the value of the critical overdensity is constant for an Einstein-de Sitter universe, in other cosmologies it can depend weakly on $\Omega_{\rm m}$ and Ω_Λ (Eke et al., 1996). In fact, this is what we find when looking at ΛCDM and $f(R)$ models. For ΛCDM, the critical overdensity is given by (Nakamura and Suto, 1997):

$$\delta_c^\Lambda(z) \simeq \frac{3(12\pi)^{2/3}}{20}\left(1 - 0.0123\log_{10}\left[1 + \frac{\Omega_m^{-1} - 1}{(1+z)^3}\right]\right)\,. \tag{2.20}$$

The modification in $f(R)$ models will be explored in Chapter 4.

2.3 Halo Mass Function

Now that we have a theory of how halos form, we want to know what the number density of halos is. If we assume that they all form from spherical collapse, we can start by estimating the number density of overdense regions that have collapsed. One way to do this is using Press-Schechter theory (Press and Schechter, 1974).

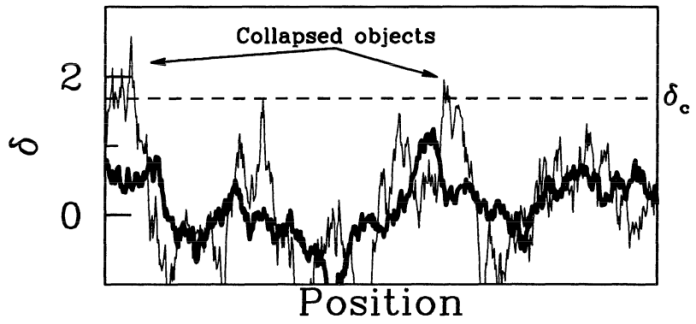

Figure 2.2: Density fluctuation field with indicated critical value (Dodelson, 2003). The dark curve represents the smoothed field.

We start with a Gaussian density fluctuation field $\delta_{\rm m}(\vec{x})$ (Figure 2.2). We can smooth this field using a top-hat filter with a smoothing scale R to get:

$$\delta_{\rm s}(\vec{x}, R) = \int d^3x' \, W_{\rm R}(\vec{x} - \vec{x}') \,, \tag{2.21}$$

where $W_{\rm R}$ is the top-hat window function:

$$W_{\rm R}(\vec{x} - \vec{x}') = \begin{cases} 1, & |\vec{x} - \vec{x}'| < R \,; \\ 0, & \text{otherwise} \,. \end{cases} \tag{2.22}$$

The probability that our Gaussian field at some point exceeds the critical value $\delta_{\rm c}$ is then given by:

$$P_{>\delta_c}(M) = \int_{\delta_c}^{\infty} \frac{2}{\sqrt{2\pi}\,\sigma(R,z)} \exp\left[-\frac{\delta_{\rm s}^2}{2\sigma^2(R,z)}\right] d\delta_{\rm s} \,, \tag{2.23}$$

where we have somewhat artificially added a factor of two to account for underdense regions and obtain the correct normalization. This is related to the so called cloud-in-cloud problem (Peacock and Heavens, 1990; Bond et al., 1991; Avelino and Viana, 2000). For more details on this problem, and a full derivation of the Press-Schechter theory, see eg. Desjacques et al. (2018).

In eq. (2.23) $\sigma(R, z)$ is the variance of the smoothed density field, obtained with linear theory. It is defined as:

$$\sigma^2_{\rm lin} = \frac{1}{2\pi^2} \int_0^{\infty} P_{\rm m}^{\rm lin}(k)\, \hat{W}_{\rm R}^2(k)\, k^2 dk \,, \tag{2.24}$$

where $\hat{W}_{\rm R}(k)$ is the Fourier transform of the real space window function $W_{\rm R}(x)$ given by eq. (2.22). $P_{\rm m}^{\rm lin}(k)$ is the linear matter power spectrum and it is the Fourier transform of the two-point correlation function of the linear matter perturbation field:

$$\langle \delta_{\rm m}(\vec{x})\, \delta_{\rm m}(\vec{x}) \rangle = \frac{1}{2\pi^2} \int_0^{\infty} P_{\rm m}^{\rm lin}(k)\, k^2 dk \,, \tag{2.25}$$

where k is the wavenumber and $\delta_{\rm m}$ is defined by eq. (2.1).

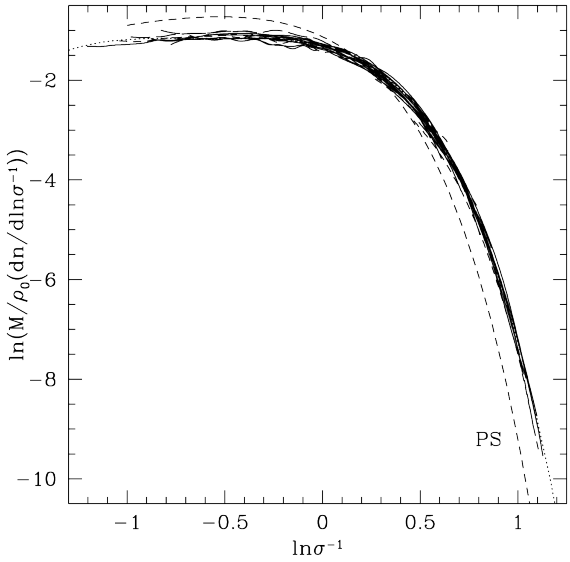

Figure 2.3: The halo mass function from numerical simulations (Jenkins et al., 2001). Dashed line is the Press–Schechter mass function.

To get the number density of halos per mass interval, we differentiate the probability in eq. (2.23) with respect to M, and multiply by the average number density $\bar{\rho}/M$. This is the Press-Schechter halo mass function, and it has the following form:

$$\frac{\mathrm{d}n(M,z)}{\mathrm{d}M} = \sqrt{\frac{2}{\pi}}\,\frac{\bar{\rho}\,\delta_c}{3\,M^2\,\sigma}\,\exp\left[-\frac{\delta_{\mathrm{s}}^2}{2\,\sigma^2(R,z)}\right]\left(-\frac{R}{\sigma}\,\frac{\mathrm{d}\sigma}{\mathrm{d}R}\right)\,. \tag{2.26}$$

It is worth noting that, even though we assume the density field is Gaussian, it is not necessarily so in reality. Looking at eq. (2.1), it is easy to see that the minimum value of δ_{m} (when $\rho_{\mathrm{m}} = 0$) is -1. As structures collapse, overdense regions easily exceed $\delta_{\mathrm{m}} = 1$, thus skewing the distribution.

While giving significant insight into the physics behind the observed distribution of halo mass in the universe, the Press-Schechter mass function does not provide a sufficiently accurate fit to N-body simulations for precision cosmology (Figure 2.3). Motivated by this, Bond et al. (1991) proposed a general form for the mass function:

$$\frac{\mathrm{d}n}{\mathrm{d}M} = f(\sigma)\frac{\bar{\rho}}{M}\frac{\mathrm{d}\ln\sigma^{-1}}{\mathrm{d}M}\,, \tag{2.27}$$

where $f(\sigma)$ is called the multiplicity or fitting function and it allows fitting of the halo mass function to simulations. Unfortunately, in reality the multiplicity function, and by extension the halo mass function, also have a slight dependency on redshift, $f(\sigma, z)$.

In this thesis, for GR, we will use the form of the multiplicity function given

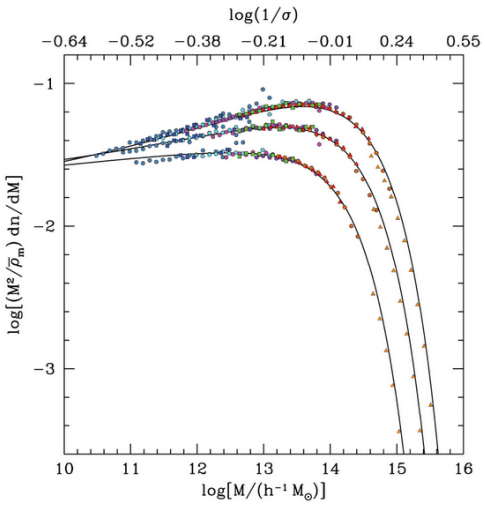

Figure 2.4: Tinker mass function fitted to simulations (Tinker et al., 2008). The three sets of points show results for density contrast values $\Delta = 200$, 800 and 3200, from top to bottom.

by (Tinker et al., 2008):

$$f(\sigma, z) = A(z) \left(\left[\frac{\sigma}{b(z)} \right]^{-a(z)} + 1 \right) \exp \left[-\frac{c(z)}{\sigma^2} \right] \tag{2.28}$$

where $A(z)$, $a(z)$, $b(z)$ and $c(z)$ are parameters that are obtained from simulations. Parameter A sets the overall amplitude of the mass function, while a and b set the slope and amplitude of the low-mass power law, respectively. Parameter c determines the cutoff scale at which the mass function starts exponentially decreasing (Figure 2.4).

These results are only valid for spherical collapse in a GR framework. As we will see in Chapter 4, once we adopt an $f(R)$ model of gravity, we will need to modify our mass function.

2.4 Halo Structure

Now that we have a way to describe the formation and abundance of dark matter halos, we will look at their internal structure. First we will focus on the distribution of dark matter density inside the halo, and then the pressure profile of the intra-cluster gas.

Since the Sunyaev-Zel'dovich effect, which is the focus of this thesis, does not depend on the formation and distribution of galaxies, we will not examine their structure nor distribution within halos.

2.4.1 Matter density profile

Cold dark matter is the dominant matter component of the halo, whose distribution dictates the gravitational potential. Assuming spherical symmetry of the halo, this distribution can be described by a radial density profile. The most common density profile used for dark matter halos is the NFW profile (Navarro et al., 1997). It is based on the Press-Schechter theory, described in Section 2.2, and assumes that halos are virialized.

The profile was obtained by fitting the output of N-body simulations and it has the following form:

$$\rho(r) = \rho_{\rm c} \frac{\delta_{\rm char}}{\frac{r}{r_{\rm s}}\left(1+\frac{r}{r_{\rm s}}\right)^2}\,, \tag{2.29}$$

where $r_{\rm s}$ is the scale radius and $\delta_{\rm char}$ is a dimensionless characteristic density which is proportional to the mean density of the universe at the time of halo formation. $\rho_{\rm c}$ is the critical density of the universe, defined by eq. (1.23).

It is useful to define here quantities relative to the density contrast Δ. For example, we define R_Δ as the radius in which the density contrast is Δ. Quantities defined with respect to this radius are then denoted with the same subscript.

If we now define a concentration parameter $c_{200} = R_{200}/r_{\rm s}$, with R_{200} the radius in which the density contrast is $\Delta = 200$, we can write the characteristic overdensity as:[1]

$$\delta_{\rm char} = \frac{200}{3}\frac{c_{200}^3}{\ln(1+c_{200}) - \frac{c_{200}}{1+c_{200}}}\,. \tag{2.30}$$

With this parametrization, the density profile of an isolated halo can be completely described by only two parameters: halo mass and the characteristic overdensity.

2.4.2 Pressure profile

The intra-cluster medium (ICM) of a dark matter halo is filled with hot gas, characterized by a pressure profile. Motivated by the fact that the gas pressure distribution is primarily determined by the dark matter inside the cluster, Nagai et al. (2007) developed a general NFW pressure profile. It is given in dimensionless form as:

$$\mathbb{p}(x) = \frac{P_0}{(x\,c_{500})^\gamma\,[1+(x\,c_{500})^\alpha]^{(\beta-\gamma)/\alpha}}\,, \tag{2.31}$$

where P_0, α, β and γ are free parameters, $x = r/r_{\rm s}$, and c_{500} is the concentration parameter defined now at radius R_{500}.

Arnaud et al. (2010) used a combination of simulations and observations from a representative sample of 33 nearby ($z < 0.2$) clusters from the REFLEX catalog

[1] R_{200} is in literature commonly referred to as the virial radius. By definition they are not strictly the same quantity, but were found to roughly coincide in a spherical collapse model (Cole and Lacey, 1996).

to determine parameters $(P_0, \alpha, \beta, \gamma)$. They found that the physical pressure is then given by:

$$P(r) = P_{500} \left[\frac{M_{500}}{3 \cdot 10^{14}\, \mathrm{h}_{70}^{-1}\, M_\odot} \right]^{\alpha_\mathrm{P} + \alpha'_\mathrm{P}(x)} \mathbb{p}\,(x)\ , \tag{2.32}$$

with a relation between α_P and α'_P:

$$\alpha'_\mathrm{P}(x) = 0.10 - (\alpha_\mathrm{P} + 0.10) \frac{(x/0.5)^3}{1. + (x/0.5)^3}\,. \tag{2.33}$$

Parameter α_P then defines the slope of the pressure profile.

Though we expect some modification of the pressure profile in case of modified gravity, we will still use Arnaud's universal pressure profile, eq. (2.32). We will address the possible modification by marginalizing over the parameter α_P.

Chapter 3

Cosmic Microwave Background

In 1965 two American scientists, Penzias and Wilson, made their first measurements with the Holmdel Horn antenna. What they accidentally discovered confirmed the Big Bang theory, earned them a Nobel prize, and ultimately ushered the scientific community into an era of precision cosmology. They reported measuring a temperature excess of (3.5 ± 1) K (Penzias and Wilson, 1965) coming from all directions in the sky, thus confirming earlier theoretical predictions of the existence of an isotropic radiation field permeating the universe (Alpher et al., 1948; Dicke et al., 1965).

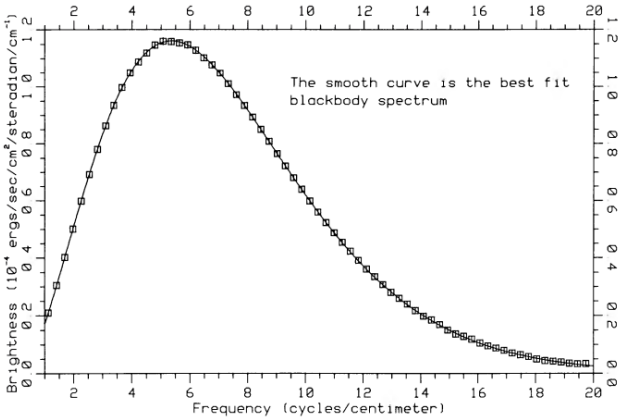

Figure 3.1: The first spectrum of the CMB obtained from FIRAS, an instrument aboard the COBE satellite (Mather et al., 1990). At this point the CMB temperature was estimated to be 2.735 K.

Measurements of the spectrum of this radiation were shown to fit a perfect black body model to an incredible degree (Figure 3.1), and the temperature estimated from this fit was 2.725 K (Mather et al., 1999). Seeing as how the peak of the spectrum was in microwave, the radiation was dubbed the Cosmic Microwave Background (CMB) radiation.

3.1 Origin of the CMB

The existence of the CMB was predicted by the Hot Big Bang theory. We have already stated that the universe is expanding, with the scale factor a getting bigger. Reversing this picture, it becomes apparent that further back in the past it had to have been smaller and smaller. In fact, if we go back enough, the scale factor goes to zero, a singularity. This is what gave rise to the Big Bang theory. In this theory the universe was hot and dense at early times, gradually expanding and cooling as time went on. Though at first so hot that only elementary particles existed, it eventually cooled down enough to allow the existence of baryons. At that point space was filled with a hot mix of electrons, baryons and photons which coupled together forming a photon-baryon fluid. The photons in this dense mix frequently scattered off of the free electrons via Thomson scattering, resulting in a very short mean free path of the photons — the light was trapped. These frequent interactions also resulted in thermodynamic equilibrium between matter and light.

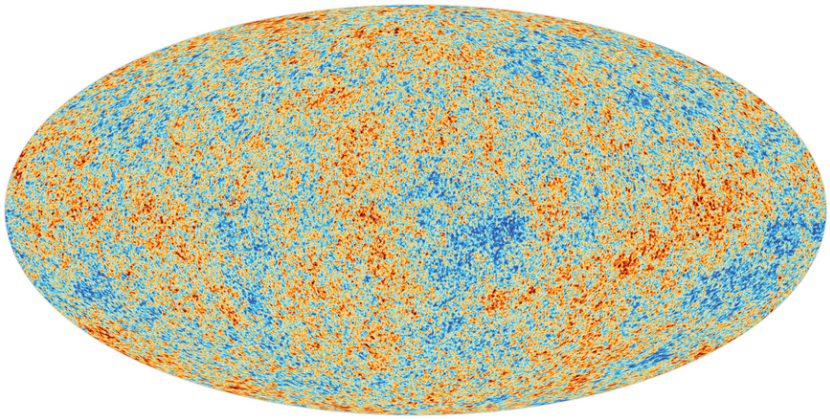

Figure 3.2: The CMB temperature map from *Planck* (ESA and The *Planck* Collaboration)

As the universe cooled off more, at a temperature around 3 000 K, it was finally cold enough for protons and electrons to recombine and form atoms. As the number of free electrons diminished, the photons were able to free-stream away. As we look out into the universe, and thus into the past, we can see these photons coming from the surface of a sphere centered around our position. This is the "last scattering surface".

A consequence of the thermodynamic equilibrium that was in place before recombination, is that the radiation coming from the last scattering surface retains a black body spectrum. The spectral energy density radiated by a black body at temperature T and frequency ν, is given by Planck's law (Planck, 1900):

$$u_\nu(T)d\nu = \frac{8\pi h\nu^3}{c^3}\frac{d\nu}{e^{\frac{h\,\nu}{k_\mathrm{B}T}} - 1}\,. \tag{3.1}$$

From here we can obtain the energy density by integrating eq. (3.1) over all

frequencies:

$$u = \frac{8\,\pi^5\,k_{\rm B}^4}{15\,c^3\,h^3}\,T^4\,, \tag{3.2}$$

where h and $k_{\rm B}$ are Planck's and Boltzmann's constant, respectively.[1] Since the equation of state parameter for radiation is $w = 1/3$, from eq. (1.29) follows that $u \propto a^{-4}$. Combining this with eq. (3.2), we find how temperature evolves with the scale factor:

$$T \propto \frac{1}{a}\,. \tag{3.3}$$

Knowing the photon temperature at recombination and the CMB temperature today, it is easy to get the scale factor at the time of recombination as $T_{\rm CMB}/T_{\rm rec} \approx 0.0009$. This gives a redshift value of $z_{\rm rec} \approx 1100$.

3.2 Temperature Anisotropies

Though the CMB temperature field is incredibly isotropic (so much so that it caused the "horizon problem" in cosmology), there are in fact small deviations from this isotropy. They were first observed with COBE and were found to be of order of 10^{-6} K (Smoot et al., 1992). Let us define such anisotropies in some direction $\vec{n}$ in the sky:

$$\Theta(\vec{n}) = \frac{T(\vec{n}) - \bar{T}}{\bar{T}}\,, \tag{3.4}$$

where $T(\vec{n})$ is the temperature in that direction, and $\bar{T}$ is the average CMB temperature. Since the radiation is coming from the surface of a sphere, we expand eq. (3.4) using spherical harmonics, to get:

$$\Theta(\vec{n}) = \sum_{\ell=2}^{\infty} \sum_{m=-l}^{\ell} a_{\ell m}\, Y_{\ell m}(\vec{n})\,. \tag{3.5}$$

In the above equation $a_{\ell m}$ are the harmonic coefficients, and $Y_{\ell m}$ are the spherical harmonics, defined as:

$$Y_{\ell m}(\vec{n}) = \sqrt{\frac{2\ell+1}{4\pi}\frac{(\ell-m)!}{(\ell+m)!}}P_\ell^m(\cos\theta)e^{im\phi}\,, \tag{3.6}$$

where $P_\ell(\theta)$ are the associated Legendre polynomials.

Note that we start the sum in eq. (3.5) from multipole value $\ell = 2$. This is because the monopole ($\ell = 0$) and the dipole ($\ell = 1$) do not give us information about intrinsic anisotropies. The monopole describes the mean value of the temperature across the entire sky, while the dipole is the result of our movement through space, relative to the CMB.

Assuming the fluctuations that gave rise to temperature anisotropies are Gaussian, the harmonic coefficients will also have a Gaussian distribution with zero mean value. The variance of the coefficients is then given by:

$$\langle a_{\ell m} a^*_{\ell' m'} \rangle = \delta_{\ell\ell'}\delta_{mm'}\,C_\ell\,, \tag{3.7}$$

where C_ℓ is called the **angular power spectrum**.

[1] Here we use the usual notation for energy density, u, but note that this is the same quantity as ρ_r.

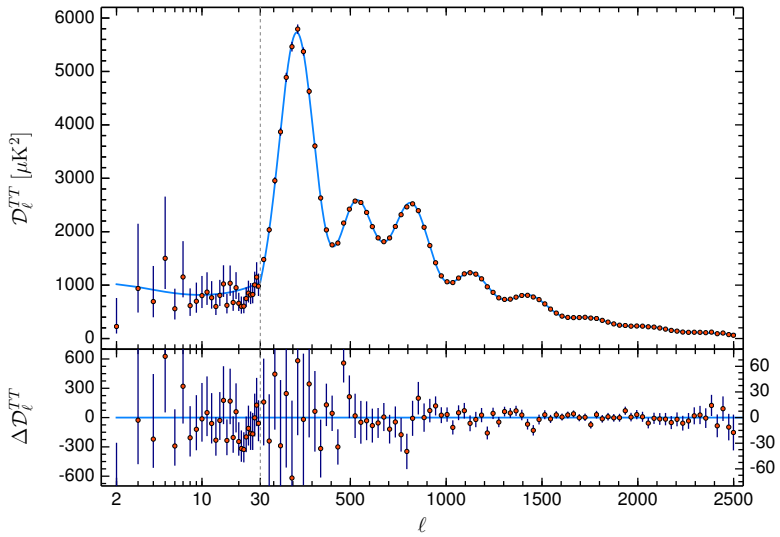

Figure 3.3: *Planck* 2015 results for the temperature power spectrum fitted with the ΛCDM model (top panel) and residuals (bottom panel) (Aghanim et al., 2018). D_ℓ^{TT} is defined as $D_\ell^{TT} = \ell(\ell+1)\,C_\ell\,/\,(2\pi)$.[2]

The power spectrum is in fact the Fourier space equivalent of the two-point correlation function, which is defined as:

$$C(\theta) \;=\; \langle\, \Theta(\vec{n}_1)\,\Theta(\vec{n}_2)\,\rangle\;, \tag{3.8}$$

where θ is the angle between vectors $\vec{n}_1$ and $\vec{n}_2$, and brackets indicate that we average over the whole sky. In simple terms, if we measure a temperature fluctuation $\Theta(\vec{n}_1)$, the two-point correlation function tells us how probable it is to measure fluctuation $\Theta(\vec{n}_2)$ separated by an angular distance θ.

If we now plug in the definition for the temperature fluctuations, eq. (3.5), into eq. (3.8), we get:

$$C(\theta) = \sum_\ell \frac{2\ell+1}{4\pi} C_\ell P_\ell(\theta)\,. \tag{3.9}$$

After COBE, WMAP and *Planck* missions (Figure 3.3) gave increasingly better measurements of the power spectrum. This allows us to better constrain cosmological models by relating the parameters to the power spectrum. To do this, however, we first need to know the physics of how the anisotropies formed.

3.2.1 Intrinsic anisotropies

Intrinsic anisotropies are ones that were formed due to effects that were happening immediately before or at the time of recombination. These effects include

[2]The superscript "*TT*" signifies that we are looking at the temperature power spectrum. There are also polarization power spectra, but they are not relevant for the purpose of this thesis.

perturbations in the gravitational potential and adiabatic perturbations.

Gravitational perturbations will give two opposing contributions to the temperature anisotropies. Firstly, a photon that was in a gravitational well during recombination will lose energy climbing out — it is gravitationally redshifted. At the same time, perturbations in the gravitational potential also cause time dilation effects, so the same photon will look "younger" and lose less energy due to subsequent expansion of the universe, eq. (3.3). The sum of these effects is commonly known as the **Sachs-Wolf effect** (Sachs and Wolfe, 1967) and it affects the power spectrum at large scales (low multipoles).

Adiabatic perturbations, on the other hand, happen because of fluid dynamics. We already mentioned that baryons, photons and electrons were coupled together before recombination, and acted as a perfect photon-baryon fluid. Gravitational perturbations then induced perturbations in the density distribution of this fluid, eq. (2.4). At the same time, radiation pressure acts as a restoring force against the density perturbations, resulting in oscillations through the fluid. This effect causes the **acoustic peaks**, the most prominent feature of the power spectrum (Figure 3.3).

3.2.2 Secondary anisotropies

Secondary anisotropies (also known as late-time anisotropies) are produced on the photon's journey from the last scattering surface to the observer. We will cover only some of these effects, for a more comprehensive list see eg. Hu (1995)

The Integrated Sachs-Wolf effect is a consequence of the expansion of the universe. Expansion drives the decay of large scale structures and their gravitational potentials. As a photon enters a potential well, it gains energy through gravitational blueshift. Since the time it takes for it to pass through the potential is larger than the rate of decay, it "sees" the potential as shallower and loses less energy on its way out. This results in a net gain of energy (Sachs and Wolfe, 1967). The reverse is true in case of a gravitational "hill".

Gravitational lensing is an effect that is simply a consequence of GR and photons traveling along geodesics. As light passes by a massive object, it is deflected by the perturbed gravitational potential and bends around it. This also happens to CMB photons as they pass massive galaxies and clusters, and we can see it as a distortion in the CMB temperature and polarization maps (Blanchard and Schneider, 1987).

The Sunyaev-Zel'dovich effect consists of two effects: thermal and kinetic Sunyaev-Zel'dovich (SZ) effect. Both of these are a result of inverse Compton scattering of low energy CMB photons off of hot electrons in galaxy clusters (Sunyaev and Zeldovich, 1972). The kinetic SZ effect is essentially a Doppler shift due to the motion of these electrons with respect to the CMB.

Since the thermal SZ effect is of particular interest for this thesis, we will consider it in a separate section.

3.3 Thermal Sunyaev-Zel'dovich effect

As we already mentioned in Section 2.4, the intra-cluster medium is filled with hot gas. The high energy electrons in this gas emit X-ray radiation that can be observed and used to study the structure of the cluster. Moreover, Sunyaev and Zeldovich (1972) showed that these electrons also interact with the low energy CMB radiation that passes through the cluster.

When CMB photons pass through the ICM, they interact with the hot electrons via inverse Compton scattering. In this process, electrons transfer some of their energy to the CMB photons, thus boosting them to higher energies. Since the total number of photons is conserved, this results in a lower number of low energy photons and an increase in the number of the higher energy ones, distorting the shape of the initially black body spectrum.

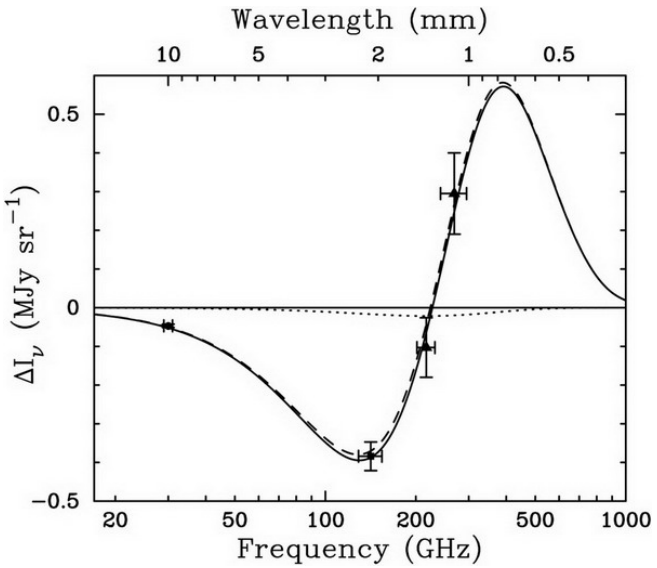

Figure 3.4: The change in CMB intensity due to SZ effect in cluster Abell 2163 (LaRoque et al., 2002). The dashed and dotted line are the best fits for thermal and kinetic SZ respectively, while the solid line is the combined effect.

Scattering in a cluster of mass M, at redshift z, results in a temperature change ΔT at angular position $\vec{\theta}$ with respect to the center of the cluster:

$$\frac{\Delta T(\vec{\theta}, M, z)}{T_{\rm CMB}} = g_\nu(x)\; y\,(\vec{\theta}, M, z)\,, \tag{3.10}$$

where $g_\nu(x)$ is the SZ spectral function:

$$g_\nu(x) = \left[x \coth\left(\frac{x}{2}\right) - 4\right] \quad \text{with} \quad x = \frac{h\nu}{k_{\rm B}\, T_{\rm CMB}}\,. \tag{3.11}$$

From the roots of this equation we can obtain that, for CMB temperature of 2.725 K, at frequencies above 217 GHz the change in temperature is positive, and for values below — it is negative (Figure 3.4).

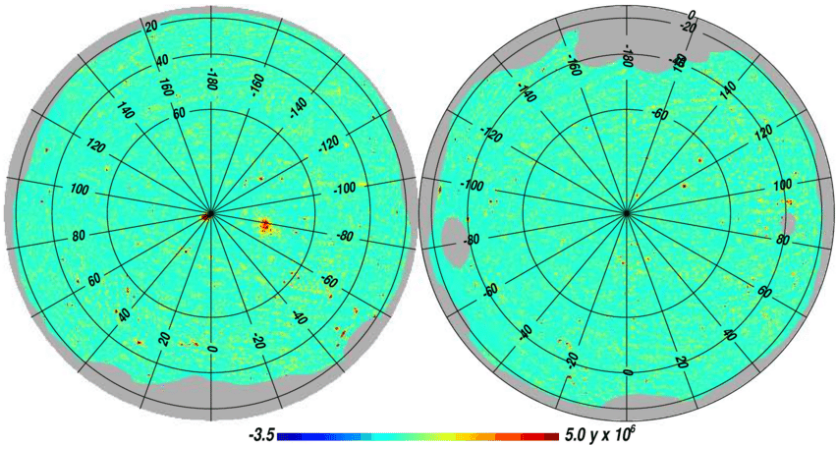

Figure 3.5: Reconstructed Planck all-sky y-Compton map (Aghanim et al., 2016)

The quantity $y\left(\vec{\theta}, M, z\right)$ is known as the Compton y-parameter and it is defined as:

$$y(\vec{\theta}, M, z) = \frac{\sigma_{\mathrm{T}}}{m_{\mathrm{e}} c^2} \int n_{\mathrm{e}} k_{\mathrm{B}} T_{\mathrm{e}} \, \mathrm{d}l = \frac{\sigma_{\mathrm{T}}}{m_{\mathrm{e}} c^2} \int P_{\mathrm{e}} \left(\sqrt{l^2 + d_{\mathrm{A}}^2 |\vec{\theta}|^2}, M, z \right) \mathrm{d}l \,, \quad (3.12)$$

where σ_{T} is the Thomson cross section, and the integral runs along the line of sight. m_{e}, T_{e}, n_{e} and P_{e} are the electron mass, temperature, number density and pressure, respectively.

Since the thermal Sunyaev-Zel'dovich effect (tSZ) is a product of scattering in clusters, it can trace the cluster distribution. This is why it is commonly used to construct cluster catalogs (Ade et al., 2016; Bleem et al., 2015). However, besides ICM pressure, the tSZ effect also depends on cosmological parameters and can be used to constrain them (Ade et al., 2016).

The amplitude of the thermal SZ power spectrum, for example, depends on Ω_{m} and σ_8 (Komatsu and Seljak, 2002). Parameter σ_8 is defined as the variance of density fluctuations, eq. (2.24), on a scale $R = 8\,h^{-1}$Mpc. It essentially represents amplitude of the linear matter fluctuations and provides a way to normalize the matter power spectrum. It is an important parameter that can be used to model the cluster mass function but attempts to constrain it using cluster counts and weak lensing revealed that it is degenerate with Ω_{m} (Huterer and White, 2002). This degeneracy can be broken by eg. combining SZ cluster counts to different datasets (Ade et al., 2016), or using higher order statistics, such as the tSZ power spectrum (Komatsu and Seljak, 2002) or bispectrum (Crawford et al., 2014).

Chapter 4

Modified Gravity

As we have already established earlier in this thesis, the universe is currently undergoing a phase of accelerated expansion. In the ΛCDM cosmological model, this expansion is explained by introducing a new form of energy with negative pressure — dark energy.

Though it is possible that this dark energy is in fact a cosmological constant, a scalar term that Einstein himself initially added to the Einstein equations, its exact nature remains unknown. Assuming that we are in fact dealing with the cosmological constant, we are also faced with the "cosmological constant problem", a discrepancy between its theoretical and observed value.[1] Additionally, there is evidence for an early epoch of accelerated expansion, called inflation, that is usually explained by an additional scalar field (Guth, 1981), proof of which has yet to be found.

All this led people to try and find an alternative explanation for accelerated expansion that would account for both of these epochs (Nojiri and Odintsov, 2003). Instead of adding exotic new forms of energy to the universe, one could try and modify the components that we already know. Attempts to modify gravity on large scales, for example, gave birth to a plethora of new **modified gravity** (MG) models. One such class of models are the ones we will explore in this thesis, the so-called $f(R)$ models.

4.1 $f(R)$ Gravity

As we have already mentioned in Section 1.2, the evolution of spacetime is described by the Einstein equations, which can be derived by varying the Einstein-Hilbert (EH) action, eq. (1.13). For a universe with a cosmological constant Λ, the EH action is given by:

$$S = \int d^4x\sqrt{-g}\left(\frac{R+2\Lambda}{16\pi G} + \mathcal{L}_{\mathrm{m}}\right). \tag{4.1}$$

As we see, the Lagrangian here is a linear function of the Ricci scalar R.

[1] for a review on the cosmological constant, see (Carroll, 2001)

Buchdahl (1970) proposed modifying gravity by making the Lagrangian into some general function of R, hence the name $f(R)$. The action would then be:

$$S = \int d^4x\sqrt{-g}\left(\frac{f(R)+R}{16\pi G} + \mathcal{L}_{\rm m}\right). \tag{4.2}$$

By varying this action, we obtain the modified Einstein equations:

$$G_{\mu\nu} + f_R R_{\mu\nu} - \left(\frac{f(R)}{2} - \Box f_R\right) g_{\mu\nu} - \nabla_\mu\nabla_\nu f_R = 8\pi G\, T_{\mu\nu}\,, \tag{4.3}$$

where $T_{\mu\nu}$ is the energy-momentum tensor and $G_{\mu\nu}$ is the Einstein tensor, defined as $G_{\mu\nu} \equiv R_{\mu\nu} - 1/2\, R\, g_{\mu\nu}$.

We see that the modification of the action also results in an additional scalar field, f_R, which is defined as:

$$f_R \equiv \frac{{\rm d}f(R)}{{\rm d}R}\,. \tag{4.4}$$

This field is coupled to matter and it is what drives the expansion. The trace of equation 4.3 will give us evolution equation for the field:

$$3\Box f_R - R + f_R R - 2f(R) = -8\pi G\,\rho\,, \tag{4.5}$$

where ρ is the density of the energy content of the universe.

4.1.1 The Hu-Sawicki $f(R)$ Model

We see from equations (4.1) and (4.2) that $f(R)$ is essentially a more general theory of gravity that, for $f(R) = 2\Lambda$, reduces to GR with a cosmological constant. What we want, however, is to find some non-linear function of R that will produce ΛCDM expansion history *without* the need for dark energy. One such family of functions was proposed by Hu and Sawicki (2007). They define a set of broken power law functions:

$$f(R) = -m^2\frac{c_1(R/m^2)^n}{c_2(R/m^2)^n + 1}\,, \tag{4.6}$$

parametrized by the slope $n > 0$, and two dimensionless normalization parameters c_1 and c_2. The mass scale is given by:

$$m^2 \equiv \frac{8\pi G\bar{\rho}_0}{3}\,, \tag{4.7}$$

where $\bar{\rho}_0$ is the average matter density today.

In the next section, where we focus on structure formation, we will be interested in regions where curvature is high compared to the mass scale. In this case we can Taylor expand eq. (4.6) to get:

$$\lim_{m^2/R\to 0} f(R) \approx -\frac{c_1}{c_2}\,m^2 + \frac{c_1}{c_2^2}\,m^2\left(\frac{m^2}{R}\right)^n. \tag{4.8}$$

The scalar field then takes the form:

$$f_R = -n\,\frac{c_1}{c_2^2}\left(\frac{m^2}{R}\right)^{n+1}. \tag{4.9}$$

The amplitude of the field c_1/c_2^2 can be parametrized by the value of the field today through (Hu and Sawicki, 2007):

$$f_{R0} = \left.\frac{\mathrm{d}f(R)}{\mathrm{d}R}\right|_{R=R_0} \approx -n\,\frac{c_1}{c_2^2}\left(\frac{12}{\tilde{\Omega}_m} - 9\right)^{-n-1}, \tag{4.10}$$

where R_0 is the value of the Ricci scalar today and $\tilde{\Omega}_m$ is the matter density parameter.

The Hu-Sawicki form of the $f(R)$ function allows us to tune our theory such that we recover the observed expansion history and, at the same time, satisfy local tests of gravity. Now we will explore how this is achieved with the help of the chameleon mechanism.

4.1.2 Local tests of gravity

Since we have accurate tests of general relativity on solar system scales (Bertotti et al., 2003), we have to make sure that our theory also passes these tests. The scalar field that appears in our theory, eq. (4.4), is a light field that couples to matter via Yukawa coupling, like gravity. It was shown (Chiba et al., 2007) that this coupling produces a long range fifth force that results in a modified potential around massive objects, like the Sun, and is inconsistent with solar system tests.

The range of Yukawa interaction is given by the Compton wavelength of the field, which is the inverse of its mass: $\lambda_{f_R} \equiv m_{f_R}^{-1}$. We can rewrite eq. (4.5) as:

$$\Box f_R = \frac{\partial V_{\text{eff}}}{\partial f_R}, \tag{4.11}$$

where the effective potential V_{eff} is given by:

$$\frac{\partial V_{\text{eff}}}{\partial f_R} = \frac{1}{3}\Big(R - f_R R + 2f(R) - 8\pi G\,\rho\Big). \tag{4.12}$$

The mass of the scalar field is then given by the second derivative of the effective potential:

$$m_{f_R}^2 = \frac{\partial^2 V_{\text{eff}}}{\partial f_R^2} = \frac{1}{3}\left(\frac{1+f_R}{f_{RR}} - R\right), \tag{4.13}$$

where f_{RR} is:

$$f_{RR} \equiv \frac{\mathrm{d}^2 f(R)}{\mathrm{d}R^2}. \tag{4.14}$$

For a massive scalar field, the Compton wavelength, and by extension the interaction range, is short and thus the field is "screened". Since we still need the fifth force to drive the expansion on cosmological scales, we need the field mass to be dependent on curvature of the environment. This way the field can pass solar system tests, where curvature is high, while still explaining expansion on cosmological scales, where the curvature is lower. Fields like these are called chameleon fields, and the described screening mechanism is the **chameleon mechanism** (Khoury and Weltman, 2004).

This ensures that our theory really agrees with observations in the low and high curvature limits. Interesting deviations, however, start to emerge at intermediate scales (Oyaizu, 2008). Here, $f(R)$ gravity causes modifications to large scale structure formation, something that we will explore in our work.

4.2 Structure Formation in $f(R)$

On scales at which large scale structure formation takes place, the chameleon mechanism is not yet fully in place, so the structure formation is modified with respect to GR results. We will now see how this affects the halo mass function by first modifying spherical collapse results, and subsequently taking into account also ellipsoidal collapse.

4.2.1 Modifications to spherical collapse

In Section 2.2, we looked at the spherical collapse of overdensities. We showed that there is a critical value for the overdensity which, once reached, results in the formation of a halo. Now we will see how this critical overdensity is modified in an $f(R)$ framework.

There are two main problems that we face. One is that Birkhoff's theorem is no longer applicable, due to monopole gravitational radiation being allowed in the $f(R)$ model (Faraoni, 2010). The other problem is that the gravity, through modification via the fifth force, now depends on the density of the environment. Because of this, unlike the spherical collapse in GR where the initial top-hat shape of the density profile was preserved, the density profiles in $f(R)$ do not retain their initial shape.

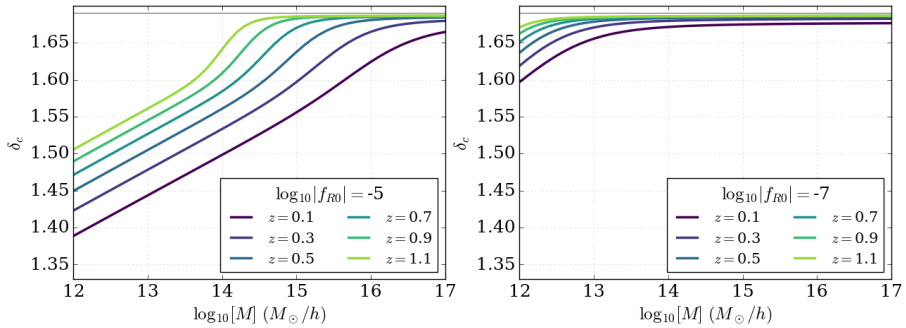

Figure 4.1: The critical overdensity obtained using eq. (4.15), for $\log|f_{R0}| = -5$ and $\log|f_{R0}| = -7$. The different lines signify halos formed at different redshift.

Kopp et al. (2013) solved the full modified field and fluid equations for the high curvature limit of the Hu-Sawicki $f(R)$ model, eq. (4.8), with $n = 1$. They preformed over a 1000 runs of their code, varying the initial overdensity δ_i, the present day value of the scalar field f_{R0} and the smoothing scale R. In the end they obtained a fitting equation for the critical overdensity, given by:

$$\delta_c(z, M, f_{R0}) = \delta_c^{\Lambda}(z)\left[1 + b_2\,(1+z)^{-a_3}\left(m_b - \sqrt{m_b^2+1}\right) + \right.$$
$$\left. + b_3\,(\tanh m_b - 1)\right] \tag{4.15}$$

where the parameters are defined as:

$$\begin{aligned} m_b(z, M, f_{R0}) &= (1+z)^{a_3} \left(\log_{10}[M/(M_\odot h^{-1})] - m_1(1+z)^{-a_4}\right) ; \\ m_1(f_{R0}) &= 1.99 \log_{10}|f_{R0}| + 26.21 ; \\ b_2 &= 0.0166 ; \\ b_3(f_{R0}) &= 0.0027 \cdot (2.41 - \log_{10}|f_{R0}|) ; \\ a_3(f_{R0}) &= 1 + 0.99 \exp\left[-2.08(\log_{10}|f_{R0}| + 5.57)^2\right] ; \\ a_4(f_{R0}) &= (\tanh\left[0.69 \cdot (\log_{10}|f_{R0}| + 6.65)\right] + 1)\, 0.11 . \end{aligned} \tag{4.16}$$

In eq. (4.15), $\delta_c^\Lambda(z)$ is the critical overdensity for ΛCDM, as defined in eq. (2.20). In both the high-redshift and high-mass limit, the $f(R)$ critical overdensity converges to the ΛCDM one. Additionally, as f_{R0} goes to zero (Figure 4.1), it converges to the constant Einstein-de Sitter solution given by eq. (2.19).

4.2.2 Modifications to the halo mass function

As we have stated before, the halo mass function can be written as eq. (2.27), with the cosmology dependence contained in the multiplicity function $f(\sigma)$. In the Press-Schechter approach we considered spherical collapse with the threshold given by a constant barrier $B = \delta_c$. For **ellipsoidal collapse**, however, the barrier is not constant and can be modeled as a stochastic process with a Gaussian distribution with mean $\bar{B}$ and variance $\sigma^2 D_B$. Here σ^2 is given by eq. (2.24), while the mean $\bar{B}$ and the diffusion coefficient D_B are free parameters and are fitted to N-body simulations. Sheth et al. (2001) extend this model by defining a barrier with a linearly drifting mean of the form:

$$\bar{B} = \delta_c + \beta\sigma^2 , \tag{4.17}$$

with β being the drifting parameter.

In that case, the multiplicity function for ellipsoidal collapse is given by:

$$f_{sk}(\sigma) = \sqrt{\frac{2a}{\pi}} \exp\left[-\frac{a\bar{B}^2}{2\sigma^2}\right] \frac{\delta_c}{\sigma} , \tag{4.18}$$

where $a = 1/(1 + D_B)$ (Kopp et al., 2013). The subscript "sk" here denotes that this form of the function is valid *only* for an overdensity field smoothed with a sharp-k filter, which is a top-hat filter in k space. [2]

As the mass of our halos is enclosed in a sphere in real space, we want to smooth our field with a real space top-hat filter (a sharp-x filter), like in Section 2.3. In this case we introduce a correction to the multiplicity function, with an amplitude parameter κ (Maggiore and Riotto, 2010).

The multiplicity function for GR, given to first order in κ, is then (Corasaniti and Achitouv, 2011):

$$f_{sx}^{\mathrm{GR}}(\sigma) = f_{sk}^{\mathrm{GR}}(\sigma) + f_{1,\beta=0}^{m-m}(\sigma) + f_{1,\beta^{(1)}}^{m-m}(\sigma) + f_{1,\beta^{(2)}}^{m-m}(\sigma) , \tag{4.19}$$

[2] Note that this is a filter which has a top-hat shape in k space, as opposed to a Fourier transform of a real space top-hat filter.

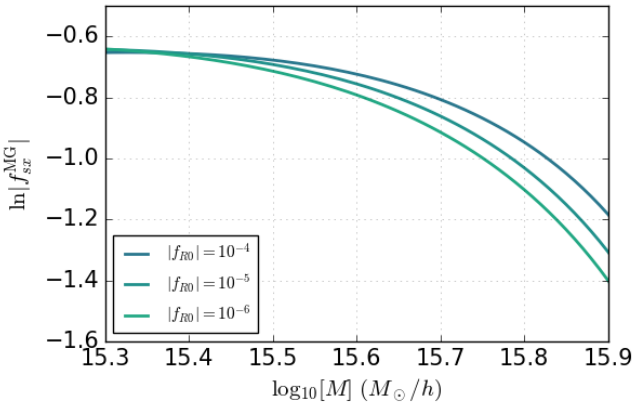

Figure 4.2: The multiplicity function, eq. (4.24), for $f(R)$ gravity with different values of $f_{\rm R0}$.

with

$$f_{1,\beta=0}^{m-m}(\sigma) = -\tilde{\kappa}\frac{\delta_c}{\sigma}\sqrt{\frac{2a}{\pi}}\left[e^{-\frac{a\delta_c^2}{2\sigma^2}} - \frac{1}{2}\Gamma\left(0, \frac{a\delta_C^2}{2\sigma^2}\right)\right], \tag{4.20}$$

$$f_{1,\beta^{(1)}}^{m-m}(\sigma) = -a\,\delta_c\,\beta\left[\tilde{\kappa}\ \mathrm{Erfc}\left(\delta_c\sqrt{\frac{a}{2\sigma^2}}\right) + f_{1,\beta=0}^{m-m}(\sigma)\right], \tag{4.21}$$

$$f_{1,\beta^{(2)}}^{m-m}(\sigma) = -a\,\beta\left[\frac{\beta}{2}\sigma^2 f_{1,\beta=0}^{m-m}(\sigma) + \delta_c\, f_{1,\beta^{(1)}}^{m-m}(\sigma)\right], \tag{4.22}$$

and $\tilde{\kappa}$ defined as $\tilde{\kappa} = \kappa/(1+D_B)$.

Let us assume that in $f(R)$ we can also write the sharp-x multiplicity function as a correction of the sharp-k function. The ratio of the GR and $f(R)$ multiplicity functions is then:

$$\frac{f_{sx}^{\rm MG}(\sigma)}{f_{sx}^{\rm GR}(\sigma)} = \frac{f_{sk}^{\rm MG}(\sigma)}{f_{sk}^{\rm GR}(\sigma)} + \mathcal{O}(\kappa^2)\,. \tag{4.23}$$

Ignoring the higher order κ correction terms, the multiplicity function for $f(R)$ is:

$$f_{sx}^{\rm MG}(\sigma) \simeq f_{sx}^{\rm GR}(\sigma)\frac{f_{sk}^{\rm MG}(\sigma)}{f_{sk}^{\rm GR}(\sigma)}\,, \tag{4.24}$$

with $f_{sk}(\sigma)$ calculated using eq. (4.18) and the corresponding critical overdensity δ_c, given by eq. (2.20) for GR, and eq. (4.15) for $f(R)$.

Chapter 5

Statistical Description

The goal of this thesis is to calculate the power spectrum and bispectrum of the Sunyaev-Zel'dovich effect in $f(R)$ gravity, and do a Fisher forecast to determine how well these two observables can constrain modified gravity models. Though we briefly mentioned the power spectrum in Section 3.2, we did not go into any details. Here we will take a closer look at spherical decomposition, and at the power spectrum, bispectrum, and their covariances. We will then use these to construct a Fisher matrix for an ideal, cosmic variance limited experiment.

5.1 The Fisher Matrix

A Fisher forecast is used to estimate how well a particular experiment can constrain a parameter through some observed quantity. The forecast makes use of the Fisher information matrix F, whose components are defined as (Heavens, 2009; Dodelson, 2003):

$$F_{ij} = \left\langle -\frac{\partial^2 (ln\,\mathcal{L})}{\partial p_i\, \partial p_j} \right\rangle , \tag{5.1}$$

where $\mathcal{L}$ is the likelihood function, and p_i and p_j are the parameters we want to constrain. The Fisher matrix is therefore a $n \times n$ matrix, with n being the number of parameters.

In simple terms, the likelihood describes the probability to obtain specific data given a theory. If the likelihood has a well defined maximum centered around the true value of the parameters, it can usually be locally approximated by a Gaussian. The derivative in the Fisher matrix looks at the curvature of the likelihood, with larger curvature corresponding to smaller variance.

In case of Gaussian distributed data and rotational invariance of the observable (Verde, 2010), the Fisher matrix can also be written as:

$$F_{ij} = \frac{\partial \mathcal{O}}{\partial p_i}^T \mathbf{Cov}(\mathcal{O})^{-1} \frac{\partial \mathcal{O}}{\partial p_j} , \tag{5.2}$$

where $\partial\mathcal{O}/\partial p_i$ is a gradient and $\mathbf{Cov}(\mathcal{O})$ is the covariance matrix of the observables.

Once the Fisher matrix is calculated, its inverse will then give us the covariance matrix for the parameters. The diagonal elements of the covariance matrix

are the uncertainties in the parameters, σ_{ii}^2, while the off-diagonal elements σ_{ij}^2 (for $i \neq j$) measure the covariance between parameters p_i and p_j.

5.2 Spherical Decomposition

Like the CMB temperature map in Section 3.2, any observable $\mathcal{O}$ on a sphere in direction $\vec{n}(\theta, \phi)$, can be decomposed into spherical harmonics, since they represent an orthonormal basis on the sphere:

$$\mathcal{O}(\vec{n}) = \sum_{\ell=0}^{\infty} \sum_{m=-l}^{\ell} a_{\ell m}\, Y_{\ell m}(\vec{n})\,, \tag{5.3}$$

with $\ell \in \mathbb{N}$ being the multipole, and $-\ell < m < \ell$ being the azimuthal parameter. The spherical harmonics are given by eq. (3.6) and satisfy the following orthonormality condition:

$$\int \mathrm{d}^2\vec{n}\, Y_{\ell m}(\vec{n})\, Y^*_{\ell' m'}(\vec{n}) = \delta_{\ell\ell'}\, \delta_{mm'}\,. \tag{5.4}$$

It is useful at this point to also define a product of two spherical harmonics, decomposed into the harmonic basis using the Gaunt coefficients $G^{\ell_1\ell_2\ell_3}_{m_1m_2m_3}$:

$$Y_{\ell_1 m_1}\, Y_{\ell_2 m_2} = \sum_{\ell_3 m_3} G^{\ell_1\ell_2\ell_3}_{m_1m_2m_3} Y^*_{\ell_3 m_3}\,. \tag{5.5}$$

The Gaunt coefficients are given by:

$$G^{m_1m_2m_3}_{\ell_1\ell_2\ell_3} = \int \mathrm{d}^2\vec{n}\, Y_{\ell_1 m_1}\, Y_{\ell_2 m_2}\, Y_{\ell_3 m_3} = \sqrt{N_{123}} \begin{pmatrix} \ell_1 & \ell_2 & \ell_3 \\ m_1 & m_2 & m_3 \end{pmatrix}, \tag{5.6}$$

with

$$\sqrt{N_{123}} = \sqrt{\frac{(2\ell_1+1)+(2\ell_2+1)+(2\ell_3+1)}{4\pi}} \begin{pmatrix} \ell_1 & \ell_2 & \ell_3 \\ 0 & 0 & 0 \end{pmatrix}, \tag{5.7}$$

where $\begin{pmatrix} \ell_1 & \ell_2 & \ell_3 \\ m_1 & m_2 & m_3 \end{pmatrix}$ are the Wigner $3j$ symbols. They are used to describe quantum systems with coupled angular momenta and can be related to Clebsch-Gordan coefficients (Wigner, 1959). An interesting property for the Wigner $3j$ symbols is that they are zero unless the following conditions are satisfied:

$$\ell_1 + \ell_2 + \ell_3 = 2n \quad n \in \mathbb{N} \tag{5.8}$$

$$|\ell_1 - \ell_2| \leq \ell_3 \leq \ell_1 + \ell_2\,, \tag{5.9}$$

$$m_1 + m_2 + m_3 = 0\,. \tag{5.10}$$

This will soon become important in our definition of the bispectrum.

5.3 Power Spectrum

Assuming statistical isotropy of the universe, the angular correlation functions should be rotationally invariant (Hu, 2001). This means that we can build an estimator by averaging over the whole sky. For the power spectrum we then have:

$$C_\ell = \frac{1}{2\ell+1}\sum_m a_{\ell m} a^*_{\ell m}\,, \tag{5.11}$$

where the factor $2\ell+1$ comes from the fact that for any given ℓ there are $2\ell+1$ values of m. This is the optimal estimator for the power spectrum, meaning that it has the smallest possible error bars. It is worth noting that this is true only for full-sky coverage and high multipoles ($\ell \gtrsim 10$), otherwise corrections need to be made. However, since our aim is to do a Fisher forecast and not analyze actual data, these technical issues are not important for us.

To construct the Fisher matrix, we will first need the covariances for our observables. For an observable $\mathcal{O}$ the covariance is defined as:

$$\mathrm{Cov}\left(\mathcal{O}, \mathcal{O}'\right) = \langle \mathcal{O}\mathcal{O}'\rangle - \langle\mathcal{O}\rangle\langle\mathcal{O}'\rangle \tag{5.12}$$

For the power spectrum we have (Lacasa, 2013):

$$\begin{aligned}
\langle C_\ell\, C_{\ell'}\rangle &= \frac{1}{(2\ell+1)(2\ell'+1)}\sum_{mm'}\langle a_{\ell m}\, a^*_{\ell m}\, a_{\ell' m'}\, a^*_{\ell' m'}\rangle \\
&= \frac{1}{(2\ell+1)(2\ell'+1)}\sum_{m,m'}\Big[\,\langle a_{\ell m}\, a^*_{\ell m}\rangle\,\langle a_{\ell' m'}\, a^*_{\ell' m'}\rangle + \\
&+ \langle a_{\ell m}\, a_{\ell' m'}\rangle\,\langle a^*_{\ell m}\, a^*_{\ell' m'}\rangle + \langle a_{\ell m}\, a^*_{\ell' m'}\rangle\,\langle a_{\ell' m'}\, a^*_{\ell m}\rangle + \\
&+ \langle a_{\ell m}\, a^*_{\ell m}\, a_{\ell' m'}\, a^*_{\ell' m'}\rangle_c\,\Big] \\
&= \langle C_\ell\rangle\,\langle C_{\ell'}\rangle + \delta_{\ell\ell'}\,\frac{2C_\ell\, C_{\ell'}}{2\ell+1} + \frac{\mathcal{P}^{(4)}(\ell,\ell,\ell',\ell',\ell^d=0)}{4\pi}\,,
\end{aligned} \tag{5.13}$$

where δ_{ij} is the Kronecker delta. In the last term $\mathcal{P}^{(4)}$ is the trispectrum (related to the connected four-point correlation function). If the four multipoles of the trispectrum form a quadrilateral in phase space, ℓ^d is the diagonal.

Since the *Planck* 2015 results lack trispectrum and pentaspectrum measurements (Aghanim et al., 2016), and our goal is to eventually make use of the *Planck* y-maps, we will focus only on two-point and three-point statistics and will not include higher order spectra.

The covariance is then given by:

$$\mathrm{Cov}(C_\ell, C_{\ell'}) = \frac{2C_\ell\, C_{\ell'}}{2\ell+1}\,\delta_{\ell\ell'}\,. \tag{5.14}$$

For Gaussian fields, most of the information is contained in the power spectrum. We are, however, interested the tSZ signal, which is produced by large scale structure. As we mentioned previously, structure formation induces non-Gaussianity in the matter density field, thus making the tSZ signal highly non-Gaussian. This means that higher-order statistics, like the bispectrum, are worth exploring as there is a lot of information contained in them.

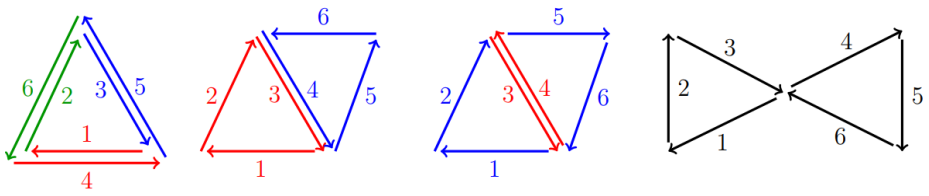

Figure 5.1: Diagrams corresponding to the different terms of the bispectrum covariance. From left to right $2 \times 2 \times 2$ (double-circulation triangle), 3×3 (parallel kite), 4×2 (opposite kite) and 6 (butterfly) (Lacasa, 2013).

5.4 Bispectrum

The bispectrum is the harmonic transform of the real space three-point correlation function. It is therefore a function of three multipoles, and it is given by:

$$B^{m_1 m_2 m_3}_{\ell_1 \ell_2 \ell_3} \equiv \langle a_{\ell_1 m_1} a_{\ell_2 m_2} a_{\ell_3 m_3} \rangle \ . \tag{5.15}$$

We can build an estimator for the bispectrum by averaging over the whole sky, just like we did for the power spectrum. The angle averaged bispectrum is then given by:

$$B_{\ell_1 \ell_2 \ell_3} \equiv \sum_m \begin{pmatrix} \ell_1 & \ell_2 & \ell_3 \\ m_1 & m_2 & m_3 \end{pmatrix} a_{\ell_1 m_1} a_{\ell_2 m_2} a_{\ell_3 m_3} \ . \tag{5.16}$$

In this thesis we will be working with the **reduced bispectrum** which is related to the angle averaged bispectrum by (Hu, 2000):

$$\begin{aligned} b_{\ell_1 \ell_2 \ell_3} &\approx \frac{1}{\sqrt{N_{123}}} B_{\ell_1 \ell_2 \ell_3} \\ &= \frac{1}{\sqrt{N_{123}}} \sum_m \begin{pmatrix} \ell_1 & \ell_2 & \ell_3 \\ m_1 & m_2 & m_3 \end{pmatrix} a_{\ell_1 m_1} a_{\ell_2 m_2} a_{\ell_3 m_3} \ . \end{aligned} \tag{5.17}$$

In eq. (5.17) and (5.16) we see that the bispectrum contains a Wigner $3j$ symbol. From the previous section we know that the symbols, and therefore the bispectrum, are zero unless conditions (5.8)–(5.10) are met. In the allowed configurations, the three multipoles (ℓ_1, ℓ_2, ℓ_3) will then form **triangles** in Fourier space. The rotational invariance of the bispectrum also demands that the bispectrum remains the same no matter how this triangle is oriented. This means that the bispectrum does not depend on the order of the multipoles, only on the **shape** of the triangle (eg. $b_{\ell_1 \ell_2 \ell_3} = b_{\ell_2 \ell_1 \ell_3}$).

Before we continue onto determining the covariance, let us define $b_{123} \equiv b_{\ell_1 \ell_2 \ell_3}$ and $a_1 \equiv a_{\ell_1 m_1}$, to shorten the notation. We then write the covariance of the bispectrum as:

$$\mathrm{Cov}(b_{123}, b_{456}) = \langle b_{123}\, b_{456} \rangle - \langle b_{123} \rangle \langle b_{456} \rangle \ . \tag{5.18}$$

Using Wick's theorem (Wick, 1950), we can split $\langle b_{123}\, b_{456} \rangle$ into four terms:

$$\langle a_{1\ldots6} \rangle = \langle a_{1\ldots6} \rangle_{(2\times2\times2)} + \langle a_{1\ldots6} \rangle_{(3\times3)} + \langle a_{1\ldots6} \rangle_{(4\times2)} + \langle a_{1\ldots6} \rangle_c \ , \tag{5.19}$$

with the subscript numbers specifying the n-point correlation function contributing to the term. We see that the last two terms have contributions from the trispectrum and the pentaspectrum. As we did previously, we will ignore the higher order spectra and focus only on the first two terms.

The first term has a power spectrum contribution and is diagonal:

$$\left\langle b_{123}^2 \right\rangle_{2\times2\times2} = \frac{1}{N_{123}} C_{\ell_1} C_{\ell_2} C_{\ell_3} \, \delta_{\ell_1\ell_2\ell_3} \,, \tag{5.20}$$

where

$$\delta_{\ell_1\ell_2\ell_3} = \begin{cases} 6 & \text{if } \ell_1 = \ell_2 = \ell_3 \\ 1 & \text{if } \ell_1 \neq \ell_2 \neq \ell_3 \\ 2 & \text{else} \end{cases} \tag{5.21}$$

This is also called the Gaussian term as it is the only non-vanishing term in case of weak non-Gaussianity (Komatsu and Spergel, 2001).The second term depends on the bispectrum itself:

$$\begin{aligned} \langle b_{123}, b_{456} \rangle_{3\times3} = \; & \frac{b_{156}\, b_{234}}{2\ell_1+1}\delta_{\ell_1\ell_4} + \frac{b_{146}\, b_{235}}{2\ell_1+1}\delta_{\ell_1\ell_5} + \frac{b_{145}\, b_{236}}{2\ell_1+1}\delta_{\ell_1\ell_6} \\ & + \frac{b_{134}\, b_{256}}{2\ell_2+1}\delta_{\ell_2\ell_4} + \frac{b_{135}\, b_{246}}{2\ell_2+1}\delta_{\ell_2\ell_5} + \frac{b_{136}\, b_{245}}{2\ell_2+1}\delta_{\ell_2\ell_6} \\ & + \frac{b_{124}\, b_{356}}{2\ell_3+1}\delta_{\ell_3\ell_4} + \frac{b_{125}\, b_{346}}{2\ell_3+1}\delta_{\ell_3\ell_5} + \frac{b_{126}\, b_{345}}{2\ell_3+1}\delta_{\ell_3\ell_6} + \langle b_{123} \rangle \, \langle b_{456} \rangle \,, \end{aligned} \tag{5.22}$$

where δ_{ij} is again the Kronecker delta. The last term, $\langle b_{123} \rangle \, \langle b_{456} \rangle$, cancels out with the one in the definition of the covariance, eq. (5.18).

The covariance of the bispectrum, ignoring correlators of higher order, is then:

$$\begin{aligned} \mathrm{Cov}(b_{123}, b_{456}) = \; & \frac{1}{N_{123}} C_{\ell_1} C_{\ell_2} C_{\ell_3} \, \delta_{\ell_1\ell_2\ell_3} \\ & + \frac{b_{156}\, b_{234}}{2\ell_1+1}\delta_{\ell_1\ell_4} + \frac{b_{146}\, b_{235}}{2\ell_1+1}\delta_{\ell_1\ell_5} + \frac{b_{145}\, b_{236}}{2\ell_1+1}\delta_{\ell_1\ell_6} \\ & + \frac{b_{134}\, b_{256}}{2\ell_2+1}\delta_{\ell_2\ell_4} + \frac{b_{135}\, b_{246}}{2\ell_2+1}\delta_{\ell_2\ell_5} + \frac{b_{136}\, b_{245}}{2\ell_2+1}\delta_{\ell_2\ell_6} \\ & + \frac{b_{124}\, b_{356}}{2\ell_3+1}\delta_{\ell_3\ell_4} + \frac{b_{125}\, b_{346}}{2\ell_3+1}\delta_{\ell_3\ell_5} + \frac{b_{126}\, b_{345}}{2\ell_3+1}\delta_{\ell_3\ell_6} \end{aligned} \tag{5.23}$$

For a full expression of the bispectrum covariance, including higher orders, we refer the reader to Chapter 2 of Lacasa (2013).

5.5 Displaying the Bispectrum

While the power spectrum is fairly easy to display as a plot of $C_\ell(\ell)$, the bispectrum depends on a configuration of three multipoles. This leads to some difficulties when trying to adequately display it.

Recall that the intensity of the bispectrum depends on the triangle configuration, rather than its orientation. We would therefore like a way to group specific triangle configurations together. One way is to simply choose and plot

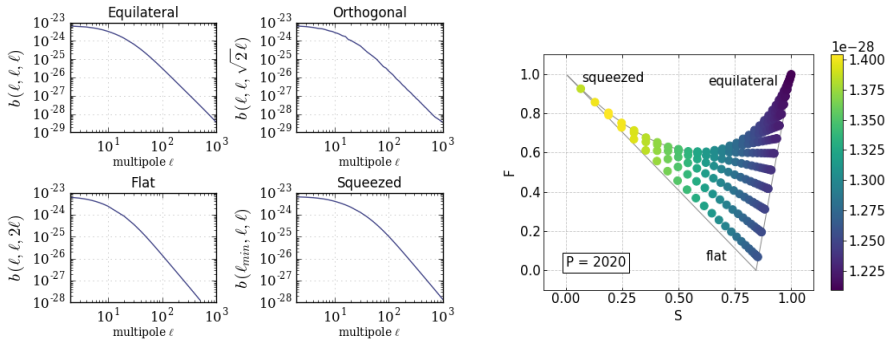

Figure 5.2: Left: Bispectrum for ΛCDM cosmology (using *Planck* 2018 parameters (Aghanim et al., 2018)), with four different types of triangles plotted separately. Right: The same bispectrum plotted using the (P, F, S) parametrization, for $P = 2020$, and with indicated positions of specific triangle configurations.

a couple of specific triangles, like all equilateral or all squeezed triangles (Figure 5.2, left). This means that we a priori choose which configurations to look at, while possibly missing important data from different configurations.

While there have been several alternative ways proposed for visualizing the bispectrum (Fergusson et al., 2012; Bucher et al., 2010), in this thesis we will adopt a parametrization proposed by Lacasa et al. (2012). This will allow us to visualize how the bispectrum changes for different triangle configurations.

We first define:

$$\sigma_1 = \ell_1 + \ell_2 + \ell_3 \,, \tag{5.24}$$

$$\sigma_2 = \ell_1\ell_2 + \ell_1\ell_3 + \ell_2\ell_3 \quad \text{and} \quad \tilde{\sigma}_2 = 12\,\frac{\sigma_2}{\sigma_1^2} - 3\,, \tag{5.25}$$

$$\sigma_3 = \ell_1\,\ell_2\,\ell_3 \quad \text{and} \quad \tilde{\sigma}_3 = 27\,\frac{\sigma_3}{\sigma_1^3}\,. \tag{5.26}$$

The new parametrization will then be based on parameters (P, F, S), defined using (σ_1, $\tilde{\sigma}_2$, $\tilde{\sigma}_3$) as:

$$P = \sigma_1\,, \tag{5.27}$$

$$F = 32\,\frac{\tilde{\sigma}_2 - \tilde{\sigma}_3}{3} + 1\,, \tag{5.28}$$

$$S = \tilde{\sigma}_3\,. \tag{5.29}$$

Parameter P represents the circumference of the triangle in phase space. Our plots will be slices of constant P with the different triangle configurations then clearly separated in the (F, S) plane (Figure 5.2, right).

Chapter 6

The Power Spectrum and Bispectrum of the tSZ Effect

Now that we have all the tools we need, we can move on to calculating the power spectrum and bispectrum of the thermal Sunyaev-Zel'dovich effect. To do this, we will make use of the halo model of the large scale structure described in Chapter 2. In the halo model, we assume that all the matter in the universe is contained inside halos. Furthermore, we assume that the structure of the halo itself is independent of the distribution of halos. This means that we can split an n-point correlation function into n terms, depending on where the contribution is coming from.[1]

The two-point correlation function, for example, will be divided into two terms:

1. The **one-halo term**, describing the correlation of points that sit inside the same halo, and
2. The **two-halo term**, describing the correlation of two points belonging to two different halos.

We can then write the power spectrum as a sum of these two terms:

$$C_\ell = C_\ell^{1\mathrm{h}} + C_\ell^{2\mathrm{h}} \,. \tag{6.1}$$

Equivalently, the bispectrum will have three terms:

$$b_{\ell_1\ell_2\ell_3} = b^{1\mathrm{h}}_{\ell_1\ell_2\ell_3} + b^{2\mathrm{h}}_{\ell_1\ell_2\ell_3} + b^{3\mathrm{h}}_{\ell_1\ell_2\ell_3} \,, \tag{6.2}$$

where the one-halo term now describes the correlation of *three* points that sit inside the same halo, the two-halo term describes the correlation where one of the points is in a different halo, and the three-halo term looks at the correlation of three points in three different halos. In this thesis we will only focus on the one halo term of the bispectrum, as it is the dominant component of the spectrum (Aghanim et al., 2016).

[1] For a more complete review of the halo model, see Cooray and Sheth (2002).

6.1 Halo Model for tSZ

In the flat sky limit, we can write the one- and two-halo terms of the **tSZ power spectrum** as (Komatsu and Kitayama, 1999; Hill and Pajer, 2013):

$$C_\ell^{1\mathrm{h}} = \int \mathrm{d}z \, \frac{\mathrm{d}^2V}{\mathrm{d}z\mathrm{d}\Omega} \int \mathrm{d}M \frac{\mathrm{d}n(M,z)}{\mathrm{d}M} \left|\tilde{y}_\ell(M,z)\right|^2, \tag{6.3}$$

$$C_\ell^{2\mathrm{h}} = \int \mathrm{d}z \, \frac{\mathrm{d}^2V}{\mathrm{d}z\mathrm{d}\Omega} \, P_\mathrm{m}^\mathrm{lin}(k,z) \left[\int \mathrm{d}M \, \frac{\mathrm{d}n(M,z)}{\mathrm{d}M} \, b_\mathrm{h}(M,z) \, \tilde{y}_\ell(M,z)\right]^2, \tag{6.4}$$

where $\mathrm{d}^2V/\mathrm{d}z\mathrm{d}\Omega$ is the comoving volume element per steradian, and $b(M,z)$ is the linear bias, defined as the ratio of the halo power spectrum to the matter power spectrum Tinker et al. (2010):

$$b_\mathrm{h}^2(M,z) = \frac{P_\mathrm{h}^\mathrm{lin}(k,M,z)}{P_\mathrm{m}^\mathrm{lin}(k,z)} \, . \tag{6.5}$$

Additionally, $\tilde{y}_\ell(M,z)$ is a Fourier transform of the projected y-Compton profile of a cluster, with a scale radius r_s. It is given by:

$$\tilde{y}_\ell(M,z) = \frac{4\pi r_\mathrm{s}}{l_\mathrm{s}^2} \int \mathrm{d}x \, x^2 \, y_\mathrm{3D}(z,M,x) \, \frac{\sin\left[\left(\ell+\frac{1}{2}\right)\frac{x}{l_\mathrm{s}}\right]}{\left(\ell+\frac{1}{2}\right)\frac{x}{l_\mathrm{s}}} \, , \tag{6.6}$$

where x and l_s are defined as $x = r/r_\mathrm{s}$ and $l_\mathrm{s} = a(z)\chi(z)/r_\mathrm{s}$, and $\chi(z)$ is the comoving distance. The radial 3D y-Compton profile, $y_\mathrm{3D}(z,M,x)$, is given by (Komatsu and Seljak, 2002):

$$y_\mathrm{3D}(z,M,x) = 1.04 \cdot 10^{-4} \mathrm{Mpc}^{-1} \left[\frac{P_\mathrm{gas}(z,M,x)}{50\mathrm{eV\ cm}^{-3}}\right] . \tag{6.7}$$

The one-halo term of the **tSZ bispectrum** is given by (Bhattacharya et al., 2012; Hurier and Lacasa, 2017):

$$b_{\ell_1\ell_2\ell_3}^{1\mathrm{h}} = \int \mathrm{d}z \, \frac{\mathrm{d}^2V}{\mathrm{d}z\mathrm{d}\Omega} \int \mathrm{d}M \frac{\mathrm{d}n(M,z)}{\mathrm{d}M} \, \tilde{y}_{\ell_1}(M,z) \, \tilde{y}_{\ell_2}(M,z) \, \tilde{y}_{\ell_3}(M,z) \, . \tag{6.8}$$

6.2 Calculations

In the following, we will refer to results obtained for general relativity as "GR", and results for $f(R)$ modified gravity as "MG" results. Since the $f(R)$ MG model is parametrized by the value of the scalar field today, f_{R0}, we will also indicate this parameter where needed.

The cosmological parameters we used for our fiducial cosmology are from the *Planck* 2018 data release, and they are listed in Table 6.1. We are already familiar with Ω_m, Ω_Λ, H_0 and σ_8 from previous chapters. Additionally, we have A_s, which is the amplitude of scalar perturbations induced by inflation, and spectral index n_s, which gives the slope of the matter power spectrum.

For the calculations of the tSZ power spectrum and bispectrum, we use a code developed by the Padova cosmology group, which makes use of the halo model

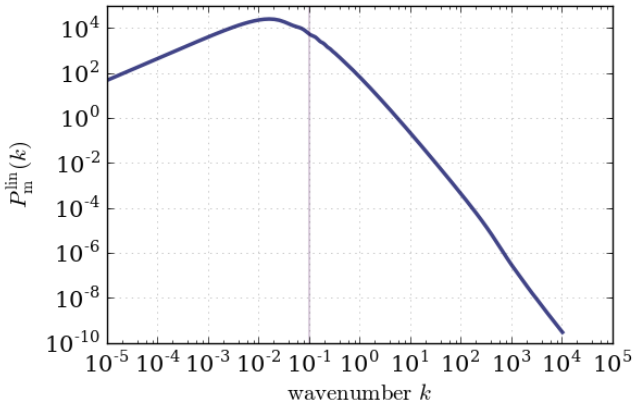

Figure 6.1: The linear matter power spectrum at redshift $z = 0$, calculated using `CLASS`. The vertical line shows the scales at which linear theory breaks down, the part on the right of this limit is obtained by extending the use of linear theory to smaller scales.

to calculate the spectra. I have modified this code and developed a pipeline for calculating bispectrum configurations beyond the equilateral one.

The code takes the matter power spectrum at redshift $z = 0$ as input, and evolves it using linear theory. For obtaining the input power spectrum in Figure 6.1, we make use of the Boltzmann code `CLASS` — the Cosmic Linear Anisotropy Solving System (Lesgourgues, 2011).

Our code then outputs the power spectrum and the bispectrum of the tSZ effect, calculated using equations (6.8) and (6.1), for multipole values from 2 and up to $\ell_{\rm max} = 1000$.

parameters	best-fit values with 1σ errors
Ω_m	0.3111 ± 0.0056
Ω_Λ	0.6889 ± 0.0056
H_0	67.66 ± 0.420
σ_8	0.8102 ± 0.0060
$10^9 A_s$	2.105 ± 0.030
n_s	0.9665 ± 0.0038

Table 6.1: Cosmological parameters from the *Planck* 2018 data release (Aghanim et al., 2018).

To carry out the bispectrum calculation, we first need to calculate the allowed triangle configurations formed by the three multipoles, (ℓ_1, ℓ_2, ℓ_3). For the multipole range of $2 < \ell < 1000$, we found that the number of the allowed configurations is $\mathcal{O}(10^7)$. Due to the long computational time required for these calculations, we had to restrict ourselves only to certain configurations. Thus we

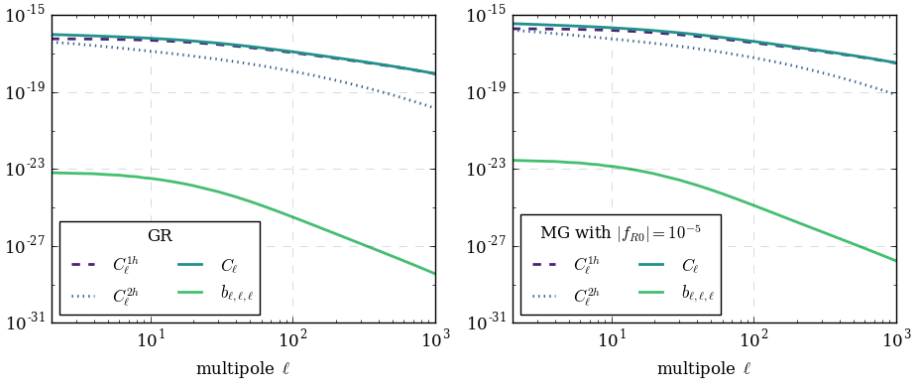

Figure 6.2: Power spectrum and diagonal bispectrum for GR (left) and MG (right)

decided to sample only some of the multipoles in our given range. Since both the power spectrum and the bispectrum vary more at lower multipoles, as seen in Figure 6.2, we choose a sampling that is more concentrated at these scales. We thus construct 67 multipole bins (Figure 6.3) with values:

1. 2 – 10 with step 1,
2. 10 – 20 with step 2,
3. 20 – 100 with step 10 and
4. 100 – 1000 with step 20.

This way we reduce the number of allowed configurations to $\mathcal{O}(10^4)$.

Since the bispectrum is smooth and varies slowly, we can use nearest-neighbor interpolation between these bins, without loosing much data.

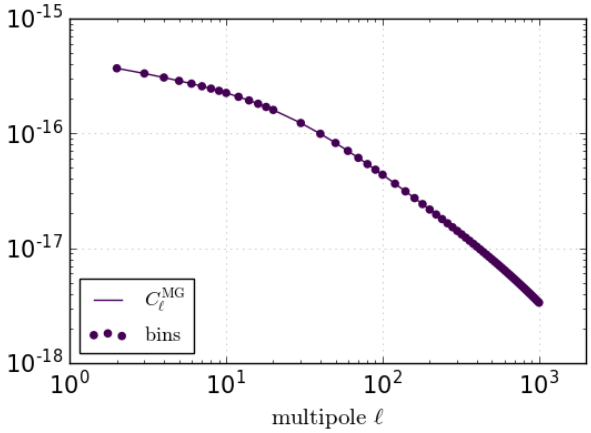

Figure 6.3: Logarithmic plot of the MG power spectrum with indicated multipole bins.

6.3 Spectra

We now present the results of our spectrum calculations.

Looking at the power spectrum in Figure 6.4, it is evident that the one-halo term is dominant, especially on small scales i.e. large multipoles. This is because, on small scales, we mainly pick up on individual clusters, so it is more likely that we look at correlation between points that belong to the same cluster.

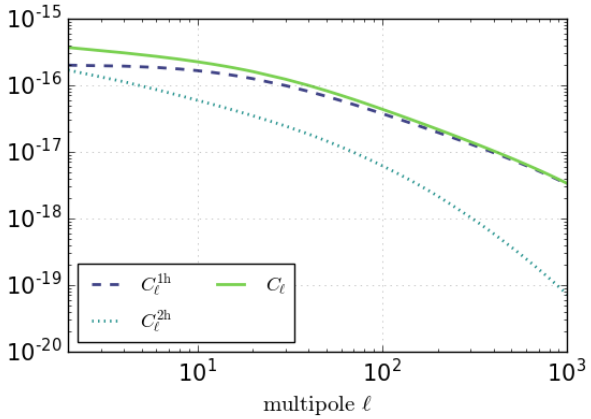

Figure 6.4: Calculated tSZ power spectrum for $f(R)$ gravity with $\log|f_{R0}| = -5$. Shown are the one- and two-halo terms, as well as the total power spectrum, $C_\ell = C_\ell^{1h} + C_\ell^{2h}$.

By considering equilateral triangle configurations of the bispectrum, we can compare it to the power spectrum. We see from Figure 6.5 that the amplitude of the power spectrum is higher than that of the bispectrum, both for MG and GR. However, while the power spectrum only has an ℓ_{max} number of contributions, we have already stated that the number of configurations is much higher for the bispectrum. This means that the total signal coming from the bispectrum can be comparable to that of the power spectrum.

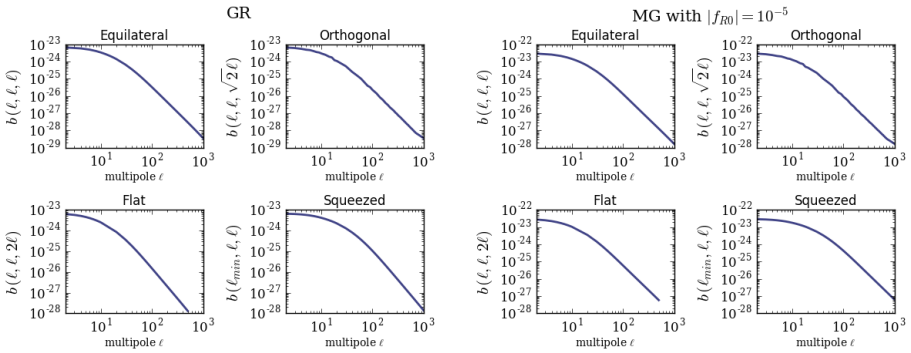

Figure 6.5: The bispectrum for different triangle configurations in case of GR (left) and MG (right)

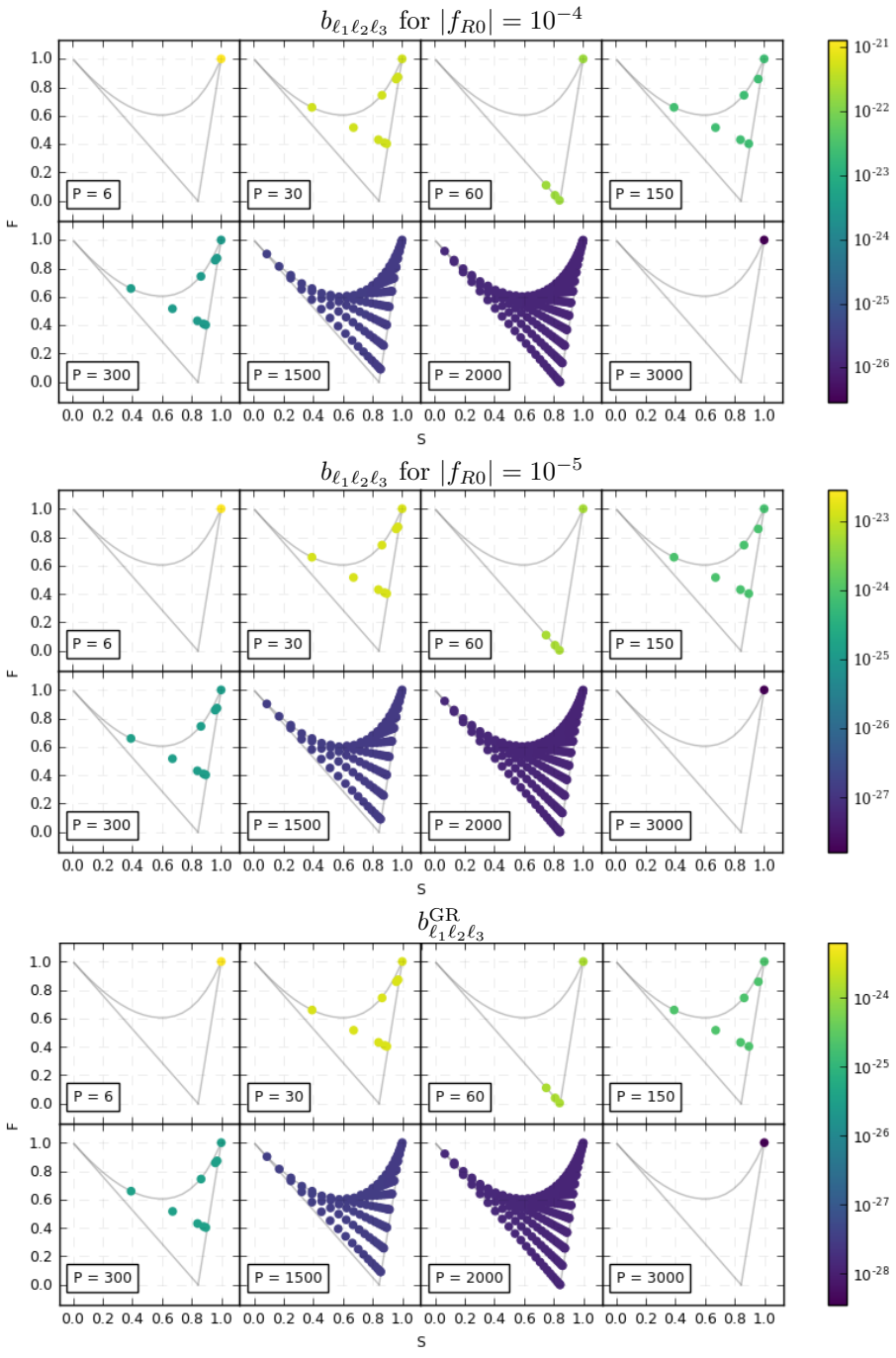

Figure 6.6: Calculated tSZ bispectrum for MG (top two panels) and GR (bottom panel). The bispectrum looks almost constant across different configurations, with the overall amplitude scaling with f_{R0}.

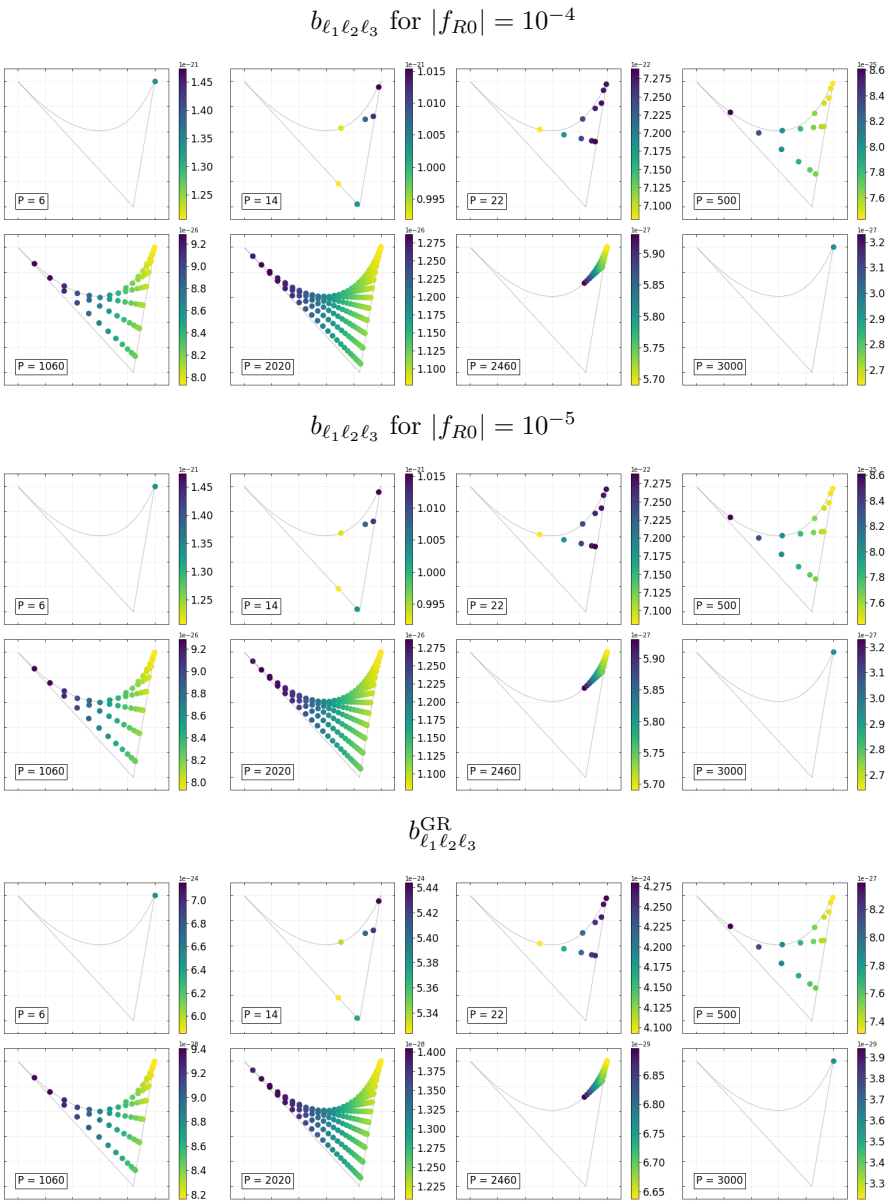

Figure 6.7: Calculated tSZ bispectrum for MG (top two panels) and GR (bottom panel). The variation of the bispectrum between different triangle configurations is visible.

Though the bispectrum can be plotted as it is in Figure 6.5, we will also plot it using the parametrization introduced in Section 5.5, to better understand its morphology. We remind the reader that parameter P represents the circumference of the phase space triangle formed by multipoles (ℓ_1, ℓ_2, ℓ_3), and the color represents the bispectrum amplitude.

In Figure 6.6 we have fixed the color scale between the different slices. Since the the variation of the bispectrum on different values of P (roughly corresponding to different scales) is much larger than any variation between different configurations, the bispectrum looks flat.

If we however look at the slices individually, we will be able to see variations of the bispectrum amplitude for different triangle configurations. We do this in Figure 6.7, where the richer morphology of the bispectrum becomes apparent.

Chapter 7

Fisher Forecast

As mentioned in Chapter 5, the goal of a Fisher forecast is to determine how well an experiment can constrain specific theories. In this thesis, we will be looking at the tSZ effect and its ability to constrain modified gravity. Though we hope to apply this procedure to *Planck* data, for now we will look at an ideal, cosmic variance limited experiment. Since cosmic variance is a statistical uncertainty, caused by the fact that we only have one Universe to observe this is the minimal uncertainty possible. This is a reasonable approximation for *Planck*, given that its data are signal-dominated up to multipole $\ell \approx 2000$, which is well within our multipole range.

7.1 Fiducial Cosmology

We choose a fiducial MG model with $|f_{R0}| = 10^{-5}$. This is based on constraints from weak lensing, that put the value of the field at $|f_{R0}| \lesssim 10^{-5}$ (Liu et al., 2016). In the special case of $f_{R0} = 0$, we recover GR.

The intra-cluster medium (ICM) is modeled using Arnaud's pressure profile, described in Section 2.4, with a free parameter $\alpha_{\rm P}$. In eq. (2.32) we saw that $\alpha_{\rm P}$ gives the slope of the pressure–mass relation; however, it is more common to look at the slope between mass and the total tSZ signal coming from a cluster, $Y_{\rm SZ}$. The total tSZ signal is obtained by integrating the gas pressure over the whole cluster, and the $Y_{\rm SZ}$–M_{500} relation is then given by:

$$\frac{Y_{\rm SZ}(R)}{Y_{500}} \propto \left[\frac{M_{500}}{3 \cdot 10^{14}\, \mathrm{h}_{70}^{-1}\, M_\odot}\right]^{\alpha_{\rm P}+\frac{5}{3}} \tag{7.1}$$

where Y_{500} is the characteristic Compton parameter, obtained by integrating over a sphere of radius R_{500}.[1] Following Arnaud et al. (2010), we set $\alpha_{\rm P} = 0.12$.

Besides the slope $\alpha_{\rm P}$, there is another free parameter coming from ICM physics, the hydrostatic mass bias b. Since the mass observed through tSZ, $M_{\rm SZ}$, is not the true mass of the cluster, it needs to be corrected using this parameter.

[1] We remind the reader that R_Δ is defined as a radius in which the density contrast is Δ (Sec 2.4).

Assuming hydrostatic equilibrium in the cluster, the mass estimated from tSZ is:

$$M_{SZ} = (1 - b)M_{500}\,. \tag{7.2}$$

Following Ade et al. (2016), we use a value for the mass bias $b = 0.2$.

7.2 Computational Difficulties

As mentioned in the previous section, the calculation of all possible triangle configurations for $\ell_1, \ell_2, \ell_3 \in [2, 1000]$ would be numerically unfeasible. To cut down on the number of calculations, we first remember that the bispectrum depends only on the shape of the triangle, not the orientation. This means we do not have to calculate all six permutations of $(\ell_1\ell_2\ell_3)$, but only one. Any sum going across all triangle configurations will then be:

$$\sum_{\ell_1\ell_2\ell_3} \;=\; 6 \sum_{2\leq\ell_1\leq\ell_2\leq\ell_3} \tag{7.3}$$

Additionally, as we mentioned, we also use a sort of binning to cut down on the number of configurations we need to calculate. As we never calculate the full bispectrum, this is not *true* binning, where the full data is obtained and then divided into bins. Instead, we calculate values only for the bins, and then do a **nearest-neighbor interpolation**. In the case of the bispectrum, this process is not trivial since all the possible triangle configurations must be assigned to their proper bins. This must be done while still respecting the triangle shape, so the bins are assigned with all three multipoles in mind (eg. configuration $(50, 925, 973)$ will go into bin $(50, 920, 960)$).

With the binning in mind, we write the Fisher matrix of the bispectrum as:

$$F_{ij} = 6 \sum_{\Delta 123} \frac{\partial b_{\Delta 123}}{\partial p_i} \mathrm{Cov}(b_{\Delta 123}, b_{\Delta 123})^{-1} \frac{\partial b_{\Delta 123}}{\partial p_j}\, \Xi_{\Delta 123}\,, \tag{7.4}$$

where bins are denoted as $\Delta\ell_1\Delta\ell_2\Delta\ell_3 \equiv \Delta 123$, and $\Xi_{\Delta 123}$ in the number of triangle configurations belonging to bin $\Delta 123$.

Finally, as we see in equation (5.2), once we calculate the covariance matrix of the bispectrum, we need to invert it. Even with the reduced amount of data, this is a computationally heavy task, as it demands an inversion of an $n \times n$ matrix, where n is the number of all possible triangle configurations. This is why, for the purposes of this thesis, we will assume **weak non-Gaussianity**. This means that the covariance of the bispectrum will be a diagonal matrix with only a power spectrum contribution. The binned covariance is then given by:

$$\mathrm{Cov}(b_{\Delta 123}, b_{\Delta 123}) \approx \frac{1}{N_{\Delta 123}}\, C_{\Delta\ell_1} C_{\Delta\ell_2} C_{\Delta\ell_3}\, \delta_{\Delta 123}\,, \tag{7.5}$$

where, assuming weak non-Gaussianity, we took the term $\langle b_{123}\rangle \langle b_{456}\rangle$ to be zero. Now our inverted matrix is simply:

$$\mathrm{Cov}^{-1}(b_{\Delta 123}, b_{\Delta 123}) \approx \frac{N_{\Delta 123}}{C_{\Delta\ell_1} C_{\Delta\ell_2} C_{\Delta\ell_3}\, \delta_{\Delta 123}}\,, \tag{7.6}$$

Note that, since $N_{\Delta 123}$ and $\delta_{\Delta 123}$ both depend on the configuration of multipoles (ℓ_1, ℓ_2, ℓ_3), we should calculate all possible configurations and then properly bin them. In the case of $\delta_{\Delta 123}$, for example, we might have a bin with three different multipoles. In this case, we know from eq. 5.21 that $\delta_{\Delta 123} = 1$. However, this bin might contain configurations where two of the multipoles are the same, so that $\delta_{123} = 2$. What we found, however, is that this does not effect the result of the Fisher analysis and, therefore, we neglect the binning and only consider the values of $N_{\Delta 123}$ and $\delta_{\Delta 123}$ for the bin itself.

7.3 Results

7.3.1 Power spectrum

We start by doing a Fisher forecast considering only the power spectrum. By varying parameters: f_{R0}, Ω_m, A_s,h, b and α_P, we obtain the results presented in Table 7.1, with the corresponding confidence ellipses shown in Figure 7.1. As we see, the constraints in this case are very weak. In the table we also give the improvements over the power spectrum results, first when using the bispectrum, and then for the combined analysis of the two. The improvement clearly illustrates the superior constraining power of the bispectrum.

parameters	fiducial	1σ	BS improvement	PSBS improvement
$10^5 f_{R0}$	1	48	$47,830\,\%$	$47,989\,\%$
Ω_m	0.3111	2.3	$187,690\,\%$	$188,810\,\%$
$10^9 A_s$	2.105	48	$57,237\,\%$	$57,539\,\%$
h	0.6766	9.0	$91,133\,\%$	$91,293\,\%$
b	0.2	29	$46,397\,\%$	$46,696\,\%$
$\alpha_{\rm P}$	0.12	8.3	$103,461\,\%$	$103,537\,\%$

Table 7.1: Fiducial values with the corresponding 1σ uncertainties obtained from the Fisher analysis of the power spectrum. The last two columns show the gained constraining power when using only the bispectrum (BS) and also the combined analysis of power spectrum and bispectrum (PSBS).

7.3.2 Bispectrum

The tSZ bispectrum has been shown to provide stronger constraints on cosmology and ICM physics than the power spectrum. Additionally, most of its signal comes from well understood massive clusters at intermediate-redshift, so it is less sensitive to astrophysical uncertainties (Bhattacharya et al., 2012). This makes the bispectrum a good potential cosmological probe, and is the reason we are considering it in this thesis.

Additionally, from equations (6.3) and (6.8), we see that the power spectrum and bispectrum have a different dependence on the y-Compton parameter, and therefore ICM physics. This means that we could break some parameter degeneracies by combining the two spectra.

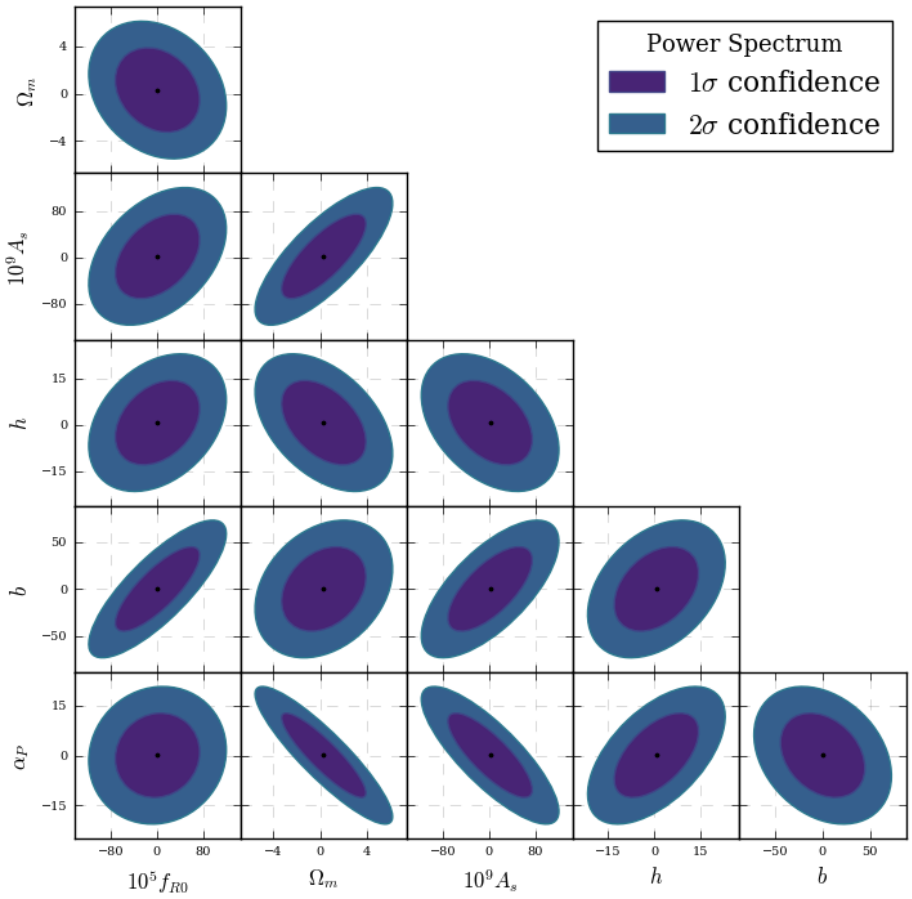

Figure 7.1: Confidence ellipses obtained from the power spectrum, with 1σ and 2σ confidence regions.

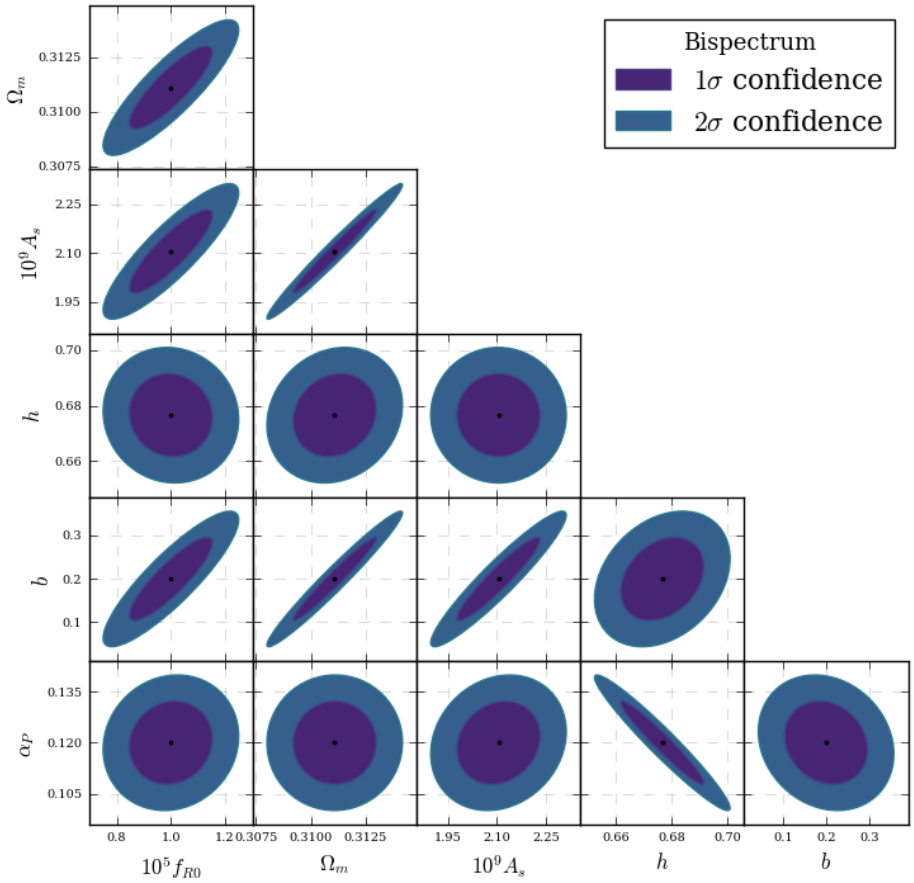

Figure 7.2: Confidence ellipses obtained from the bispectrum, with 1σ and 2σ confidence regions.

parameters	fiducial	1σ	PSBS improvement
$f_{R0} \cdot 10^5$	1.00	0.10	0.33 %
Ω_m	0.3111	0.0013	0.60 %
$A_s \cdot 10^9$	2.105	0.084	0.53 %
h	0.6766	0.0098	0.18 %
b	0.200	0.063	0.64 %
$\alpha_{\rm P}$	0.1200	0.0081	0.074 %

Table 7.2: Fiducial values with the corresponding 1σ uncertainties obtained from the Fisher analysis of the bispectrum.

We report our constraints from the bispectrum in Table 7.2, with the confidence ellipses given in Figure 7.2. As expected, the constraining power of the bispectrum far exceeds that of the power spectrum. However, we have to take into account that the we have not included any higher order spectra into the covariance.

In Figure 7.3, we also plot the derivatives of the bispectrum with respect to some of the parameters. We see that the changes are different for different triangle configurations, meaning that the bispectrum does not simply scale with changing parameters, but instead changes shape. This shows that the bispectrum alone could help in breaking some parameter degeneracies.

7.3.3 Combined power spectrum and bispectrum results

When using the tSZ effect, a major contribution in the uncertainty comes from the ICM physics. In particular, we see from Figure 7.2 that the mass bias parameter, b, is highly degenerate with cosmological parameters, including f_{R0}. As we mentioned, the combined analysis of the power spectrum and bispectrum could break those degeneracies.

parameters	fiducial	1σ
$10^5 f_{R0}$	1.00	0.10
Ω_m	0.3111	0.0012
$10^9 A_s$	2.105	0.083
h	0.6766	0.0098
b	0.200	0.063
$\alpha_{\rm P}$	0.120	0.008

Table 7.3: Fiducial values with the corresponding 1σ uncertainties obtained from the combined Fisher analysis of both the power spectrum and the bispectrum.

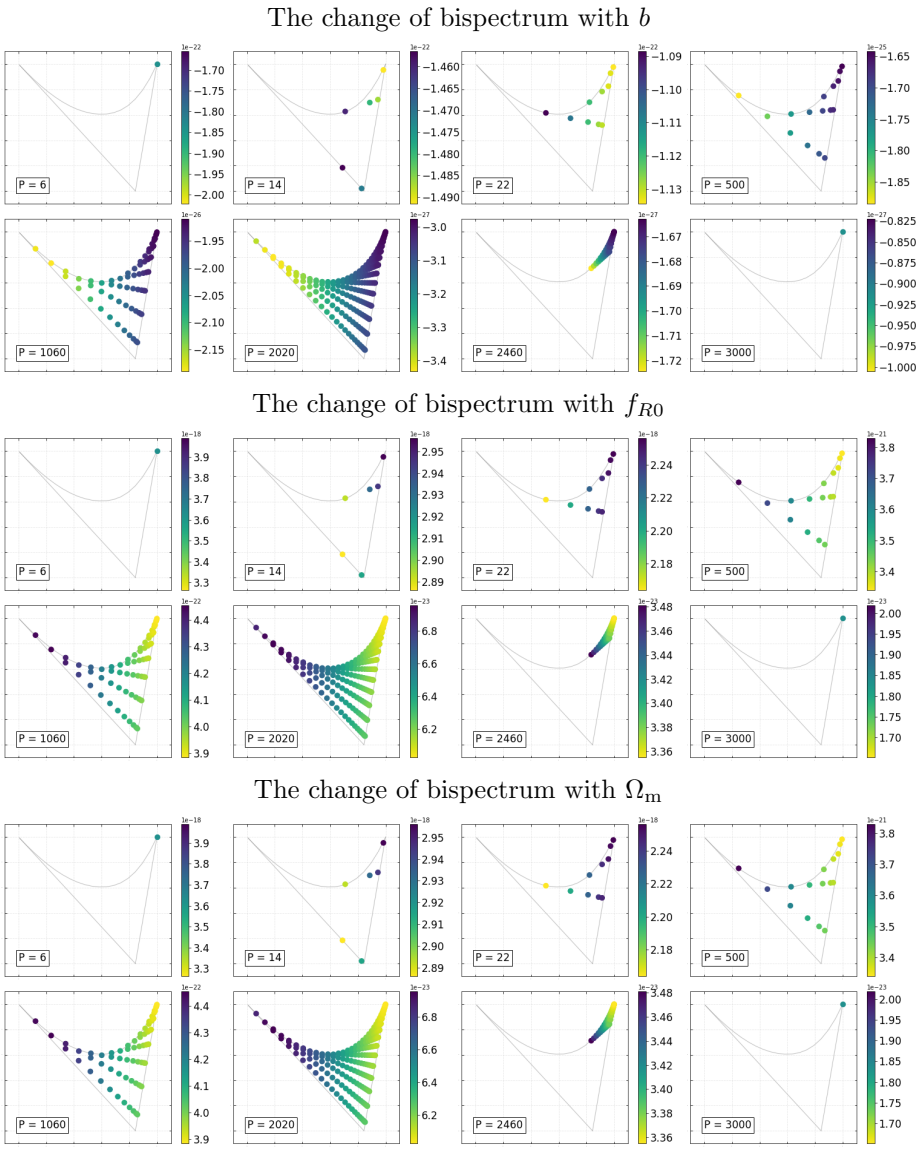

Figure 7.3: Derivative of the bispectrum with respect to mass bias b (top panel), f_{R0} (middle) and $\Omega_{\rm m}$ (bottom). We see the mass bias has most effect on equilateral configurations, while f_{R0} and $\Omega_{\rm m}$ mostly affect the squeezed ones. For the positions of specific triangles in the plot, refer to Figure 5.2.

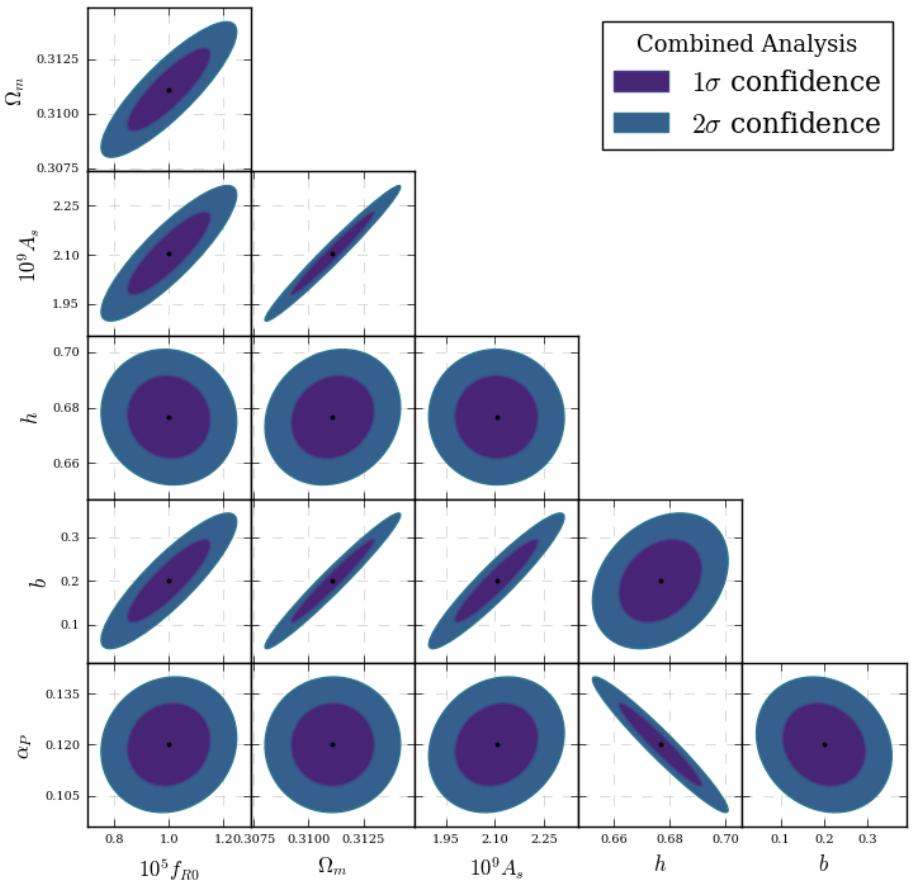

Figure 7.4: Confidence ellipses obtained from the combined analysis of both the power spectrum and the bispectrum (PSBS), with 1σ and 2σ confidence regions.

We give the results of the combined analysis in Table 7.3, with the confidence ellipses given in 7.4. We note that, as expected, the constraints are only marginally better than the bispectrum, since it is the major contributor in the Fisher matrix.

Note that the combined analysis was done by simply adding the Fisher matrices, and has not taken into account the correlation between the power spectrum and the bispectrum. This would again require inversion of a large covariance matrix, a computationally expensive task. We do, however, hope to account for this effect in the future.

Conclusion

Modified gravity models present an alternative way of explaining the accelerated expansion of the universe, without having to introduce dark energy. In this thesis in particular, we take a look at a class of modified gravity models called $f(R)$ models.

We expect $f(R)$ gravity to leave characteristic signatures in the formation of large scale structure, which could be observed. We thus introduce the theoretical tools needed to describe the formation and evolution of large scale structure in a ΛCDM model, as well as the modifications introduced by $f(R)$. We then calculate the power spectrum and bispectrum of the thermal Sunyaev-Zel'dovich effect in modified gravity, hoping to compare it to *Planck* data and thus constrain the $f(R)$ model.

To check how well we could constrain modified gravity, we first do a Fisher forecast for an ideal, cosmic variance limited experiment. Our fiducial cosmology is obtained using *Planck* 2018 cosmological parameters and modified gravity parameter $|f_{R0}| = 10^{-5}$.

First we do the analysis separately for the power spectrum and the bispectrum, and find that the constraining power of the bispectrum far exceeds the power spectrum. We also do a combined analysis using both power spectrum and the bispectrum. Here, due to computational limitations, we neglect the correlation between the two. The combined analysis then gives us a constraint on $|10^5 f_{R0}| = 1.0 \pm 0.1$.

As in this thesis we only included the power spectrum contribution while calculating the covariances of the tSZ spectra, in the future we hope to include higher order terms as well. Additionally, we also plan to adequately combine the power spectrum and bispectrum, including the correlation between the two. Due to the different dependence of the power spectrum and the bispectrum on ICM physics, this might prove helpful in breaking degeneracies between some of the ICM parameters, in particular the mass bias parameter b. This motivates the further study of tSZ spectra, beyond constraining modified gravity.

Bibliography

Ade, P. A. R. et al. Planck 2015 results. XXIV. Cosmology from Sunyaev-Zeldovich cluster counts. *Astron. Astrophys.*, 594, 2016.

Aghanim, N. et al. Planck 2015 results. XXII. A map of the thermal Sunyaev-Zeldovich effect. *Astron. Astrophys.*, 594, 2016.

Aghanim, N. et al. Planck 2018 results. VI. Cosmological parameters. 2018.

Alpher, R. A., Bethe, H., and Gamow, G. The origin of chemical elements. *Phys. Rev.*, 73, 1948.

Arnaud, M., Pratt, G. W., Piffaretti, R., Boehringer, H., Croston, J. H., and Pointecouteau, E. The universal galaxy cluster pressure profile from a representative sample of nearby systems (REXCESS) and the $Y_{SZ} - M_{500}$ relation. *Astron. Astrophys.*, 517, 2010.

Avelino, P. P. and Viana, P. T. P. The cloud-in-cloud problem for nonGaussian density fields. *Mon. Not. Roy. Astron. Soc.*, 314, 2000.

Bernardeau, F., Colombi, S., Gaztanaga, E., and Scoccimarro, R. Large scale structure of the universe and cosmological perturbation theory. *Phys. Rept.*, 367, 2002.

Bertotti, B., Iess, L., and Tortora, P. A test of general relativity using radio links with the Cassini spacecraft. *Nature*, 425, 2003.

Bhattacharya, S., Nagai, D., Shaw, L., Crawford, T., and Holder, G. Bispectrum of the Sunyaev-Zel'dovich Effect. *Astrophys. J.*, 760, 2012.

Birkhoff, G. *Relativity and modern physics*. Harvard University Press, 1923.

Blanchard, A. and Schneider, J. Gravitational lensing effect on the fluctuations of the cosmic background radiation. *Astronomy and Astrophysics*, 1842, 1987.

Blanton, M. and SDSS. SDSS Galaxy Map. URL `https://www.sdss.org/science/orangepie/`. Accessed: 2018-08-26.

Bleem, L. E. et al. Galaxy Clusters Discovered via the Sunyaev-Zel'dovich Effect in the 2500-square-degree SPT-SZ survey. *Astrophys. J. Suppl.*, 216, 2015.

Bond, J. R., Cole, S., Efstathiou, G., and Kaiser, N. Excursion set mass functions for hierarchical Gaussian fluctuations. *Astrophys. J.*, 379, 1991.

Bonnor, W. B. Jeans' Formula for Gravitational Instability. *Monthly Notices of the Royal Astronomical Society*, 117, 1957.

Buchdahl, H. A. Non-linear Lagrangians and cosmological theory. *Mon. Not. Roy. Astron. Soc.*, 150, 1970.

Bucher, M., Van Tent, B., and Carvalho, C. S. Detecting Bispectral Acoustic Oscillations from Inflation Using a New Flexible Estimator. *Mon. Not. Roy. Astron. Soc.*, 407, 2010.

Carroll, S. M. The Cosmological constant. *Living Rev. Rel.*, 4, 2001.

Chiba, T., Smith, T. L., and Erickcek, A. L. Solar System constraints to general f(R) gravity. *Phys. Rev.*, D75, 2007.

Cole, S. and Lacey, C. G. The Structure of dark matter halos in hierarchical clustering models. *Mon. Not. Roy. Astron. Soc.*, 281, 1996.

Coles, P. and Lucchin, F. *Cosmology*. John Wiley, 2002.

Cooray, A. and Sheth, R. K. Halo models of large scale structure. *Phys. Rept.*, 372, 2002.

Corasaniti, P. S. and Achitouv, I. Toward a Universal Formulation of the Halo Mass Function. *Phys. Rev. Lett.*, 106, 2011.

Crawford, T. M. et al. A Measurement of the Secondary-CMB and Millimeter-wave-foreground Bispectrum using 800 $\deg^2$ of South Pole Telescope Data. *Astrophys. J.*, 784, 2014.

Desjacques, V., Jeong, D., and Schmidt, F. Large-Scale Galaxy Bias. *Phys. Rept.*, 733, 2018.

Dicke, R. H., Peebles, P. J. E., Roll, P. G., and Wilkinson, D. T. Cosmic Black-Body Radiation. *Astrophys. J.*, 142, 1965.

Dodelson, S. *Modern Cosmology*. Academic Press, Elsevier Science, 2003.

Eke, V., Cole, S., and Frenk, C. Cluster evolution as a diagnostic for Omega. *Monthly Notices of the Royal Astronomical Society*, 282, 1996.

ESA and The *Planck* Collaboration. *Planck*'s view of the cosmic microwave background. URL `http://www.esa.int/spaceinimages/Images/2018/07/Planck_s_view_of_the_cosmic_microwave_background`. Accessed: 2018-08-31.

Faraoni, V. The Jebsen-Birkhoff theorem in alternative gravity. *Phys. Rev.*, D81, 2010.

Fergusson, J. R., Liguori, M., and Shellard, E. P. S. The CMB Bispectrum. *JCAP*, 1212, 2012.

Friedmann, A. Über die krümmung des raumes. *Zeitschrift für Physik*, 10, 1922.

Guth, A. H. The Inflationary Universe: A Possible Solution to the Horizon and Flatness Problems. *Phys. Rev.*, D23, 1981.

Heavens, A. Statistical techniques in cosmology. *ArXiv e-prints*, 2009.

Hilbert, D. Die grundlagen der physik. 1. *Gott. Nachr.*, 27, 1915.

Hill, J. C. and Pajer, E. Cosmology from the thermal Sunyaev-Zel'dovich power spectrum: Primordial non-Gaussianity and massive neutrinos. *Phys. Rev.*, D88, 2013.

Hu, W. Weak lensing of the CMB: A harmonic approach. *Phys. Rev.*, D62, 2000.

Hu, W. Angular trispectrum of the CMB. *Phys. Rev.*, D64, 2001.

Hu, W. and Sawicki, I. Models of f(R) Cosmic Acceleration that Evade Solar-System Tests. *Phys. Rev.*, D76, 2007.

Hu, W. T. *Wandering in the Background: A CMB Explorer*. PhD thesis, UC, Berkeley, 1995.

Hubble, E. A relation between distance and radial velocity among extra-galactic nebulae. *Proceedings of the National Academy of Sciences*, 15, 1929.

Hurier, G. and Lacasa, F. Combined analysis of galaxy cluster number count, thermal Sunyaev-Zel'dovich power spectrum, and bispectrum. *Astron. Astrophys.*, 604, 2017.

Huterer, D. and White, M. J. Weak lensing as a calibrator of the cluster mass-temperature relation. *Astrophys. J.*, 578, 2002.

Jenkins, A., Frenk, C. S., White, S. D. M., Colberg, J. M., Cole, S., Evrard, A. E., Couchman, H. M. P., and Yoshida, N. The Mass function of dark matter halos. *Monthly Notices of the Royal Astronomical Society*, 321, 2001.

Khoury, J. and Weltman, A. Chameleon cosmology. *Phys. Rev.*, D69, 2004.

Komatsu, E. and Kitayama, T. Sunyaev-Zel'dovich fluctuations from spatial correlations between clusters of galaxies. *Astrophys. J.*, 526, 1999.

Komatsu, E. and Seljak, U. The Sunyaev-Zel'dovich angular power spectrum as a probe of cosmological parameters. *Mon. Not. Roy. Astron. Soc.*, 336, 2002.

Komatsu, E. and Spergel, D. N. Acoustic signatures in the primary microwave background bispectrum. *Phys. Rev.*, D63, 2001.

Kopp, M., Appleby, S. A., Achitouv, I., and Weller, J. Spherical collapse and halo mass function in $f(R)$ theories. *Phys. Rev.*, D88, 2013.

Lacasa, F., Aghanim, N., Kunz, M., and Frommert, M. Characterisation of the non-Gaussianity of radio and IR point-sources at CMB frequencies. *Mon. Not. Roy. Astron. Soc.*, 421, 2012.

Lacasa, F. *Non-Gaussianity and extragalactic foregrounds to the Cosmic Microwave Background*. PhD thesis, Orsay, IAS, 2013.

LaRoque, S. J., Carlstrom, J. E., Reese, E. D., Holder, G. P., Holzapfel, W. L., Joy, M., and Grego, L. The sunyaev-zel'dovich effect spectrum of abell 2163. 2002.

Lesgourgues, J. The Cosmic Linear Anisotropy Solving System (CLASS) I: Overview. *ArXiv e-prints*, 2011.

Lifshitz, E. M. On the gravitational stability of the expanding universe. *J. Phys. (USSR)*, 16, 1946.

Liu, X. et al. Constraining $f(R)$ Gravity Theory Using Weak Lensing Peak Statistics from the Canada-France-Hawaii-Telescope Lensing Survey. *Phys. Rev. Lett.*, 117, 2016.

Longair, M. *Galaxy Formation*. Springer, 2008.

Maggiore, M. and Riotto, A. The Halo Mass Function from Excursion Set Theory. I. Gaussian fluctuations with non-Markovian dependence on the smoothing scale. *Astrophys. J.*, 711, 2010.

Mather, J. C., Fixsen, D. J., Shafer, R. A., Mosier, C., and Wilkinson, D. T. Calibrator design for the COBE far infrared absolute spectrophotometer (FIRAS). *Astrophys. J.*, 512, 1999.

Mather, J. C. et al. A Preliminary measurement of the Cosmic Microwave Background spectrum by the Cosmic Background Explorer (COBE) satellite. *Astrophys. J.*, 354, 1990.

Nagai, D., Kravtsov, A. V., and Vikhlinin, A. Effects of Galaxy Formation on Thermodynamics of the Intracluster Medium. *Astrophys. J.*, 668, 2007.

Nakamura, T. T. and Suto, Y. Strong gravitational lensing and velocity function as tools to probe cosmological parameters: Current constraints and future predictions. *Prog. Theor. Phys.*, 97, 1997.

Navarro, J. F., Frenk, C. S., and White, S. D. M. A Universal density profile from hierarchical clustering. *Astrophys. J.*, 490, 1997.

Nojiri, S. and Odintsov, S. D. Modified gravity with negative and positive powers of the curvature: Unification of the inflation and of the cosmic acceleration. *Phys. Rev.*, D68, 2003.

Oyaizu, H. Non-linear evolution of f(R) cosmologies I: methodology. *Phys. Rev.*, D78, 2008.

Peacock, J. A. and Heavens, A. F. Alternatives to the Press-Schechter cosmological mass function. *Mon. Not. Roy. Astron. Soc.*, 243, 1990.

Peirone, S., Raveri, M., Viel, M., Borgani, S., and Ansoldi, S. Constraining f(R) Gravity with Planck Sunyaev-Zel'dovich Clusters. *Phys. Rev.*, D95, 2017.

Penzias, A. A. and Wilson, R. W. A Measurement of excess antenna temperature at 4080-Mc/s. *Astrophys. J.*, 142, 1965.

Perlmutter, S. et al. Measurements of Ω and Λ from 42 High-Redshift Supernovae. *The Astrophysical Journal*, 517, 1999.

Planck, M. Zur Theorie des Gesetzes der Energieverteilung im Normalspectrum. *Verhandlungen der Deutschen Physikalischen Gesellschaft*, 2, 1900.

Press, W. H. and Schechter, P. Formation of galaxies and clusters of galaxies by selfsimilar gravitational condensation. *The Astrophysical Journal*, 187, 1974.

Riess, A. G. et al. Observational Evidence from Supernovae for an Accelerating Universe and a Cosmological Constant. *The Astronomical Journal*, 116, 1998.

Sachs, R. K. and Wolfe, A. M. Perturbations of a cosmological model and angular variations of the microwave background. *Astrophys. J.*, 147, 1967.

Sheth, R. K., Mo, H. J., and Tormen, G. Ellipsoidal collapse and an improved model for the number and spatial distribution of dark matter haloes. *Mon. Not. Roy. Astron. Soc.*, 323, 2001.

Smoot, G. F. et al. Structure in the COBE differential microwave radiometer first year maps. *Astrophys. J.*, 396, 1992.

Sunyaev, R. A. and Zeldovich, Ya. B. The Observations of relic radiation as a test of the nature of X-Ray radiation from the clusters of galaxies. *Comments Astrophys. Space Phys.*, 4, 1972.

Tinker, J. L., Kravtsov, A. V., Klypin, A., Abazajian, K., Warren, M. S., Yepes, G., Gottlober, S., and Holz, D. E. Toward a halo mass function for precision cosmology: The Limits of universality. *The Astrophysical Journal*, 688, 2008.

Tinker, J. L., Robertson, B. E., Kravtsov, A. V., Klypin, A., Warren, M. S., Yepes, G., and Gottlober, S. The Large Scale Bias of Dark Matter Halos: Numerical Calibration and Model Tests. *The Astrophysical Journal*, 724, 2010.

Verde, L. Statistical Methods in Cosmology. In *Lecture Notes in Physics, Berlin Springer Verlag*, volume 800 of *Lecture Notes in Physics, Berlin Springer Verlag*, 2010.

Wheeler, J. A. and Ford, K. W. *Geons, Black Holes, and Quantum Foam.* W. W. Norton & Company, 1998.

Wick, G. C. The Evaluation of the Collision Matrix. *Phys. Rev.*, 80, 1950.

Wigner, E. *Group theory and its applications to the quantum mechanics of atomic spectra.* Academic Press Inc. New York, 1959.